Stochastic heating of free electrons in multiple electromagnetic waves: A simple physical analysis

G Blaclard, F Quéré, G Bonnaud, H Vincenti

Stochastic heating of free electrons in multiple electromagnetic waves: A simple physical analysis

G. Blaclard,[1,2] F. Quéré,[1] G. Bonnaud,[1] and H. Vincenti[1,*]
[1]*LIDYL, CEA, CNRS, Université Paris-Saclay, CEA Saclay, 91 191 Gif-sur-Yvette, France*
[2]*Lawrence Berkeley National Laboratory, Berkeley, California 94720, USA*

(Received 18 May 2022; revised 23 December 2022; accepted 10 January 2023; published 14 March 2023)

It is established that charged particles crossing the interference field of two colliding electromagnetic (EM) waves can behave chaotically, leading to a stochastic heating of the particle distribution. A fine understanding of the stochastic heating process is crucial to the optimization of many physical applications requiring a high EM energy deposition to these charged particles. Predicting key stochastic heating features (particle distribution, chaos threshold) is usually achieved using a heavy Hamiltonian formalism required to model particle dynamics in chaotic regimes. Here, we explore an alternative and more intuitive path, which makes it possible to reduce the equations of motion of particles to rather simple and well-known physical systems such as Kapitza and gravity pendulums. Starting from these simple systems, we first show how to estimate chaos thresholds by deriving a model of the stretching and folding dynamics of the pendulum bob in phase space. Based on this first model, we then derive a random walk model for particle dynamics above the chaos threshold, which can predict major features of stochastic heating for any EM polarization and angle θ_i.

DOI: 10.1103/PhysRevE.107.034205

I. INTRODUCTION

A free electron cannot absorb photons from an electromagnetic (EM) field because such a process cannot simultaneously conserve energy and momentum. It can, however, potentially gain energy by photon scattering, because the involvement of two photons with different energies and momenta now provides enough degrees of freedom to respect both conservation laws. If the EM field consists of a single plane wave, such scattering processes are spontaneous, and they are therefore rather inefficient. By contrast, when several waves with different wave vectors and/or frequencies are present, stimulated scattering can result in efficient energy absorption. As it comes into play in very diverse contexts and conditions, the dynamics of free electrons in multiple EM waves is an important topic, which has stimulated many investigations in the past decades [1–8]. In the present work, we will concentrate on the case of the interaction with multiple intense laser beams. In this context, a situation of particular interest, due to its simplicity and experimental relevance, corresponds to the superposition of multiple waves of the same frequency, propagating along different directions. Such a superposition, for instance, occurs during the interaction of a high-power laser with a dense plasma (initially solid target) where the reflection of the incident laser wave by the target can give rise to the superposition of incident and reflected laser waves at the same central frequency in front of the target. As introduced below, we recently demonstrated that this superposition can lead to an unexpected laser absorption at very high laser intensities [7].

For EM waves of large amplitude, the electron dynamics in the field can generally be described in the nonrelativistic regime. In the case of a single EM wave, the particle nonrelativistic motion is integrable and periodic, regardless of the wave amplitude [9]. The situation can radically change when several waves are present: for high enough wave amplitudes, the particle motion can become nonintegrable, and it turns into a chaotic dynamic. In this regime, the loss of periodicity in the particle motion induces a temporal dephasing between the particle current J and the total electric field E of the waves, therefore leading to a net absorption of the EM waves energy through a nonzero average of the $\mathbf{J}\cdot\mathbf{E}$ term in Maxwell's equations. The absorption process resulting from this chaotic behavior of a free particle in multiple waves has been called stochastic heating [1], and it is expected to occur for laser intensities exceeding 10^{17} W/cm^2 [2,3,7,10].

This intensity threshold can nowadays be exceeded by up to six orders of magnitude with high-power femtosecond lasers [11]. Stochastic heating is therefore highly relevant in experiments performed with such lasers, where it can play a key role in multiple physical applications, generally calling for a maximization of the EM wave energy deposition to particles. Getting physical insight into this particle-wave coupling mechanism and making predictions of its key features (e.g., chaos onset in different interaction conditions, or resulting energy distribution of particles) is therefore timely and important.

So far, the prediction of these key features has had to rely on a rather involved mathematical approach: using the Hamiltonian formalism, conditions for chaos onset can be determined by finding all resonances of the system and checking for resonances overlaps that can lead to chaos [2,3,6,12,13]. It is usually not possible to find these resonances analytically, and the determination of chaos onset eventually requires a

*henri.vincenti@cea.fr

numerical resolution of the system evolution with an in-depth analysis of Poincaré's sections. In addition to such mathematical analysis, it is useful to get a simpler and maybe more intuitive physical insight into the wave-particle coupling and the emergence of chaos in a system whenever possible. This is precisely the goal of this article.

Here, we describe a simple physical approach to understand and predict key features of stochastic heating of free electrons in two laser waves. Our approach bridges the gap between a predictive but rather abstract Hamiltonian formalism on the one hand, and an intuitive but nonpredictive physical reasoning on the other hand. Compared to the standard Hamiltonian formalism, it provides a more straightforward physical understanding of the stochastic heating process, but it also predicts the chaos threshold as well as particle distributions. This study is divided into five parts:

(i) In Sec. I, we first briefly remind the reader of the equations of motion of a particle in EM waves, and we introduce the formalism and motion invariants that are required in the subsequent theoretical analysis.

(ii) In Sec. II, we show how to reduce these equations of motion to the ones of simple pendulums, whose nature depends on the polarization of the EM waves.

(iii) In Sec. III, we explain how the so-called stretching and folding mechanism in phase space can lead to chaotic dynamics of the particles. We then derive a first physical model for this mechanism, and we use this model to derive a threshold on the laser intensity for the onset of chaos.

(iv) In Sec. IV, we use this model to derive a random walk model of particle dynamics in two colliding waves. We show how to obtain key features of stochastic heating from this model.

(v) In Sec. V, we generalize our study to an arbitrary colliding angle θ between the two waves.

II. ELECTRON MOTION IN AN ELECTROMAGNETIC FIELD

In the remainder of this article, we will treat particles as "test particles," i.e., we will assume no particle-particle interaction and thus derive equations of motion for a single particle. The relativistic equation of motion for a single electron reads

$$\frac{d\boldsymbol{p}}{dt} = -e(\boldsymbol{E} + \boldsymbol{v} \times \boldsymbol{B}) \quad \text{and} \quad \boldsymbol{p} = m\gamma\boldsymbol{v} \tag{1}$$

with

$$\boldsymbol{E} = -\frac{\partial \boldsymbol{A}}{\partial t} \quad \text{and} \quad \boldsymbol{B} = \boldsymbol{\nabla} \times \boldsymbol{A}, \tag{2}$$

where $\mathbf{A}$ is the vector potential resulting from the superposition of all EM waves. We thus get

$$\frac{d\boldsymbol{p}}{dt} = -e\left(-\frac{\partial \boldsymbol{A}}{\partial t} + \boldsymbol{\nabla}(\boldsymbol{v}\cdot\boldsymbol{A}) - (\boldsymbol{v}\cdot\boldsymbol{\nabla})\boldsymbol{A} \right). \tag{3}$$

From now on, we will consider only plane waves propagating along the $\boldsymbol{x}$-axis, in either direction. The polarization direction lies in the transverse (y, z) plane. As the vector potential is invariant by translation in this transverse plane, Eq. (3) leads to the following equation of motion in this plane:

$$\frac{d\boldsymbol{p}_\perp}{dt} = e\left(\frac{\partial}{\partial t} + v_x\frac{\partial}{\partial x}\right)\boldsymbol{A}_\perp = e\frac{d\boldsymbol{A}_\perp}{dt}, \tag{4}$$

where the symbol $\perp$ stands for the transverse component. Equation (4) is the so-called *canonical momentum conservation* equation:

$$\frac{d}{dt}(\boldsymbol{p}_\perp - e\boldsymbol{A}_\perp) = 0 \quad \Leftrightarrow \quad \boldsymbol{p}_\perp - e\boldsymbol{A}_\perp = \mathrm{C}^{\mathrm{st}}. \tag{5}$$

$\boldsymbol{p}_\perp - e\boldsymbol{A}_\perp$ is thus found to be motion-invariant. From now on, and until the last section of this article, we will consider that electrons are initially at rest before the laser waves arrive ($p_\perp = 0$ when $\boldsymbol{A}_\perp = 0$), such that the constant on the right-hand side is zero, and

$$\boldsymbol{p}_\perp = e\boldsymbol{A}_\perp. \tag{6}$$

Based on the above equation, it is convenient to introduce the normalized laser amplitude $a_0 = eA_\perp/m_e c$. When $a_0 > 1$, $p_\perp > m_e c$, and this is called the relativistic regime of interaction between the electron and the EM field.

This equation shows that a particle initially at rest [i.e., when $\boldsymbol{A}_\perp(t \to -\infty) \to 0$] transiently gains energy in transverse directions when it interacts with plane electromagnetic waves, but restitutes all this energy to the waves at the end of the interaction [i.e., when $\boldsymbol{A}_\perp(t \to +\infty) \to 0$)]. There can be no net gain in energy by the particle *in the transverse plane* at the end of the interaction.

Since the transverse dynamics of the electron in the field cannot lead to a net energy gain, in the rest of this work we will fully concentrate on the longitudinal motion, i.e., the motion along the direction of propagation of the waves. Moreover, as we only consider plane waves, there is no longitudinal component of the vector potential. Consequently, $\mathbf{A} = \mathbf{A}_\perp$, and we therefore drop the $\perp$ notation in the remainder of this work. Following Eq. (3), the equation of motion along this axis is

$$\frac{dp_x}{dt} = -e\left(\boldsymbol{v}\cdot\frac{\partial \boldsymbol{A}}{\partial x}\right). \tag{7}$$

Using the conservation of the transverse canonical momentum in this equation, one obtains the differential equation in p_x:

$$\frac{dp_x}{dt} = -e\left(\frac{\boldsymbol{p}}{m\gamma}\cdot\frac{\partial \boldsymbol{A}}{\partial x}\right) = -\frac{e^2}{2m\gamma}\frac{\partial A^2}{\partial x}, \tag{8}$$

where $A^2 = A_y^2 + A_z^2$. The right-hand side of the equation is the so-called *ponderomotive force*. Let us now derive an equation for the longitudinal position x. To do so, we differentiate the particle velocity:

$$\begin{aligned}\frac{dv_x}{dt} &= \frac{1}{m\gamma}\frac{dp_x}{dt} - \frac{p_x}{m\gamma^2}\frac{d\gamma}{dt} \\ &= -\frac{e^2}{2m^2\gamma^2}\frac{\partial A^2}{\partial x} - \frac{e^2 v_x}{2\gamma^2 m^2 c^2}\left(\frac{dA^2}{dt} - v_x\frac{\partial A^2}{\partial x}\right).\end{aligned} \tag{9}$$

Finally, using $\dot{x} = dx/dt = v_x$ and the formula for the total derivative of A^2, the equation of motion in the relativistic regime reads

$$\frac{d^2x}{dt^2} + \frac{e^2}{2m^2\gamma^2}\left(\frac{\partial}{\partial x} + \frac{\dot{x}}{c^2}\frac{\partial}{\partial t}\right)A^2 = 0. \tag{10}$$

In the nonrelativistic limit, i.e., $a_0 \ll 1$, $\gamma \to 1$, and $|\dot{x}| \ll c$, it simply becomes

$$\frac{d^2x}{dt^2} + \frac{e^2}{2m^2}\frac{\partial A^2}{\partial x} = 0. \tag{11}$$

Equation (11) is valid for any superposition of laser plane waves propagating along x. In the next sections, we will expand A^2 for different wave configurations and exhibit the main properties of the resulting particle dynamics. In particular, we will see that motion of an electron in EM waves is analogous to that of a bob of a pendulum, the type of which depends on the polarization states of the EM waves.

III. ELECTRON DYNAMICS IN PLANE EM WAVES: A PENDULUM ANALOGY

Starting from the results of the previous section, we will now derive simple equations of motions in a few selected configurations. To simplify the calculations, we will consider only cases in which $a_0 \ll 1$, i.e., we will mainly focus on the nonrelativistic regime (in this section as well as in the following one, Sec. IV). As we will see in Sec. IV, this is justified by the fact that chaos onset occurs at $a_0 \ll 1$.

A. Electron dynamics in a single plane wave

For a better understanding of the complex particle dynamics in multiple EM waves, it is useful to start with a brief reminder of the simple case of electron motion in a *single* plane wave, linearly polarized along the z-axis:

$$\boldsymbol{A} = A_0 \sin(k_0 x - \omega_0 t)\boldsymbol{z}, \tag{12}$$

with $A_0 = a_0 mc/e$. In this case, it is possible to derive the relativistic orbits of electrons by noting that the system admits an additional motion-invariant $\gamma mc - p_x$:

$$\begin{aligned} mc\frac{d\gamma}{dt} &= -\frac{e}{c}\boldsymbol{v}\cdot\boldsymbol{E} = \frac{e}{\gamma mc}p_z\frac{\partial A_z}{\partial t} \\ &= \frac{e^2}{2\gamma mc}\frac{\partial A_z^2}{\partial t} \\ &= -\frac{e^2}{2\gamma m}\frac{\partial A_z^2}{\partial x} = \frac{dp_x}{dt} \\ &\Rightarrow \frac{d}{dt}(mc\gamma - p_x) = 0. \end{aligned} \tag{13}$$

There are thus three independent motion invariants [two from Eq. (5) and one from Eq. (13)] in a physical system with three degrees of freedom (one per spatial dimension), which makes the system integrable in the Liouville sense. As a consequence, the evolution of the system is fully predictable and cannot exhibit any chaotic behavior.

The equations of motion in the nonrelativistic regime can easily be derived from Eq. (11):

$$\frac{d^2x}{dt^2} + \frac{a_0^2c^2k_0}{2}\sin(2(k_0x - \omega_0 t)) = 0. \tag{14}$$

Let us define $\xi \to 2(k_0x - \omega_0 t)$, the position of the electron in the frame comoving at c with the EM wave. ξ satisfies the following equation:

$$\frac{d^2\xi}{dt^2} + a_0^2\omega_0^2\sin\xi = 0. \tag{15}$$

This is the equation of a *simple gravity pendulum*. The oscillation period of this pendulum would be $T = 2\pi/a_0\omega_0$ and the solution can be expressed using elliptic integrals. A particle initially at rest in the laboratory frame will start with a velocity close to the speed of light in the comoving frame, for which the pendulum bob performs complete rotations. The resulting total particle motion along the x-axis in the laboratory frame is then a combination of a periodic behavior related to the pendulum oscillations and a drift towards $x > 0$.

To illustrate this, we picture in Fig. 1(a) a plane wave, propagating towards positive $\boldsymbol{x}$ and impinging on an electron cloud initially at rest and laid out randomly within a square: $-2\,\lambda_0 \leqslant x_{t=0},\ z_{t=0} \leqslant 2\,\lambda_0$. One electron of this population is highlighted in blue, and its trajectory along time is pictured as the blue line in Fig. 1(a).

When the particles are inside the wave, they oscillate along the polarization direction. This is what leads to the deformation of the electron cloud observed in Fig. 1(a) in the ($x > 0$) half-plane. But after the wave has passed [see the ($x < 0$) half-plane], the electron cloud is observed to recover its initial square shape. This is because electrons return to rest after the passage of the EM wave, gaining no net energy. After the interaction, the electron distribution is therefore identical to its initial state, but shifted towards positive x. This induced spatial drift is clearly visible on the blue trajectory. The corresponding particle has traveled by $\simeq 3\,\lambda_0$ during the whole interaction.

Regarding the electron distribution in phase space [see Figs. 1(b) and 1(c)], it is possible to express all momentum components in terms of A_z only, starting from the formulas leading to motion invariants. For p_y and p_z, Eq. (5) gives $p_y = 0$ and $p_z = eA_z$ because the initial distribution is at rest. For p_x, we use the last invariant [see Eq. (13)]:

$$\begin{aligned} & mc\gamma - p_x = mc \\ \Leftrightarrow\quad & m^2c^2 + p_x^2 + p_y^2 + p_z^2 = (mc + p_x)^2 \\ \Leftrightarrow\quad & 2mc\,p_x = p_z^2 = e^2A_z^2. \end{aligned} \tag{16}$$

It turns out that every momentum component is known at all times and at every position. From Eq. (16) in particular, we find that p_x is always positive and oscillates at twice the laser frequency [see Fig. 1(b)]. This explains the previously described drift of electrons towards positive x. In addition, it also turns out that the relation between p_z and p_x is the equation of a parabola as illustrated in Fig. 1(c). During its evolution in phase space (p_x, p_z), an electron would just move along this parabola. At the end of the interaction, A_z returns to zero and so do p_x and p_z. Again, this shows that particles cannot gain energy in a single plane wave.

In the following, we add a second laser wave and show how it affects the electron motion.

B. Electron dynamics in two EM waves

In the nonrelativistic limit, the longitudinal equation of motion of an electron in two colliding EM waves can be

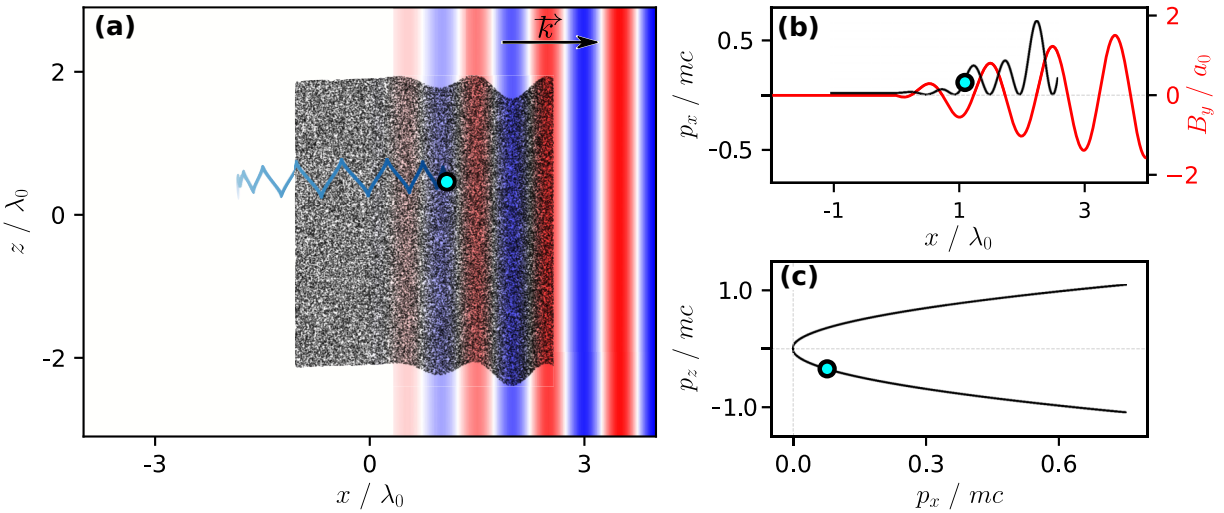

FIG. 1. Electron dynamics in a single linearly polarized EM wave. In panel (a), a snapshot at a given time t of the laser spatial profile is pictured in color scale. The laser is traveling towards positive x through a cloud of electrons (considered as noninteracting test particles) pictured as black dots. One particle is highlighted as a blue dot (in all panels), and its trajectory up to time t is shown as a blue line. In panels (b) and (c) we also display a snapshot, at the same time t, of the electron distributions in (x, p_x) and (p_x, p_z) spaces, respectively. To assist the reader, the magnetic field is plotted as well in panel (b) (red line).

written in a very simple form, similar to that of free or forced pendulums, depending on the EM wave polarizations. This analogy will turn out to be very useful to discuss the possibility of chaotic dynamics of electrons in intense waves.

Starting from Eq. (11), we write the longitudinal equation of motion for two different configurations: (i) two circularly polarized waves, and (ii) two waves linearly polarized, propagating along the same direction. Although we will show that the first configuration can never lead to chaos, it is still instructive to consider it to get some physical insight, which will help us to better understand the complex electron dynamics in the second configuration.

For the sake of simplicity, we assume that these two waves have the same angular frequency ω_0, as explained in the Introduction, but also that they have the same amplitude a_0. In Secs. III–V, we will restrict our analysis to cases in which the two waves are counterpropagating along the x-axis. The case of waves crossing at other angles will be dealt with in Sec. VI.

1. Equations of motion in two circularly polarized waves

In this case, the transverse vector potential $A_\perp$ for each wave reads

$$\begin{aligned} \boldsymbol{A}_1 &= A_0(\cos(\omega_0 t - k_0 x)\boldsymbol{y} + \sin(\omega_0 t - k_0 x)\boldsymbol{z})/\sqrt{2}, \\ \boldsymbol{A}_2 &= A_0(\cos(\omega_0 t + k_0 x)\boldsymbol{y} \pm \sin(\omega_0 t + k_0 x)\boldsymbol{z})/\sqrt{2}, \end{aligned} \tag{17}$$

where $\boldsymbol{A}_1$ corresponds to the wave propagating towards positive x, and $\boldsymbol{A}_2$ corresponds to the one propagating towards negative x. The first laser is chosen to be right-handed circularly (RHC) polarized, but the second one can either be RHC polarized [negative sign in Eq. (17), a configuration hereafter called RHC/RHC] or left-handed circularly (LHC) polarized [positive sign in Eq. (17), a configuration hereafter called RHC/LHC]. In the RHC/RHC configuration, the electric fields of both waves rotate in the same direction as one moves along the x-axis, leading to a total field with a constant amplitude along x. In contrast, in the RHC/LHC configuration, these two fields rotate in opposite directions as x changes, leading to a total field with a spatially varying instantaneous amplitude.

In the nonrelativistic limit, we only need to compute the spatial partial derivative of $A^2 = A_y^2 + A_z^2$ to get an explicit formula for Eq. (10), which reads

$$\begin{aligned} \frac{\partial A^2}{\partial x} = \frac{A_0^2}{2}\frac{\partial}{\partial x}([\cos(\omega_0 t - k_0 x) + \cos(\omega_0 t + k_0 x)]^2 \\ + [\sin(\omega_0 t - k_0 x) \pm \sin(\omega_0 t + k_0 x)]^2). \end{aligned} \tag{18}$$

After developing the inner brackets, we get

$$\frac{\partial A^2}{\partial x} = \begin{vmatrix} A_0^2 \dfrac{\partial}{\partial x}(1 + \cos(2\omega_0 t)) = 0, \\ A_0^2 \dfrac{\partial}{\partial x}(1 + \cos(2k_0 x)) = -2A_0^2 k_0 \sin(2k_0 x), \end{vmatrix} \tag{19}$$

where the first line corresponds to the RHC/RHC case, and the second one to the RHC/LHC case. Back to Eq. (10), we find

$$\frac{d^2x}{dt^2} = \begin{vmatrix} 0 & \text{in RHC/RHC}, \\ a_0^2 c^2 k_0 \sin(2k_0 x) & \text{in RHC/LHC}. \end{vmatrix} \tag{20}$$

With the change of variable $\pi + 2k_0 x \to \theta$, the temporal evolution of the system is given by

$$\begin{aligned} &\frac{d^2\theta}{dt^2} = 0 && \text{in RHC/RHC}, \\ &\frac{d^2\theta}{dt^2} + \underbrace{2a_0^2\omega_0^2}_{\omega^2}\sin\theta = 0 && \text{in RH/LHC}. \end{aligned} \tag{21}$$

When the two lasers are RHC-polarized, the first line of Eq. (21) shows that the electron is not submitted to any force along the longitudinal direction. As a result, when $v_{x|t=0} = 0$,

it does not move at all along the longitudinal direction. This statement remains valid even in the relativistic regime because the relativistic equation of motion, Eq. (8), becomes $dp_x/dt = 0$. Of course, there is still transverse dynamics, since the motion is given by the transverse component of the vector potential [cf. canonical momentum conservation, Eq. (5)]. Overall, for this polarization configuration, the motion is known at each time: $p_x = 0$ and $\boldsymbol{p}_\perp = \boldsymbol{A}$, and it will not be discussed further in the remainder of this work.

If the two laser waves now present opposite circular polarizations (RHC and LHC), we find that the equation of motion is identical to that of a simple gravity pendulum, like in the case of an electron in a single EM wave [compare Eqs. (15) and (21)]. Note, however, that these two equations hold in different frames: the longitudinal drift occurring in the case of a single wave is suppressed in the presence of two waves.

The longitudinal dynamics can be expressed using elliptic functions. The swing period of the corresponding pendulum would be $T = 2\pi/\omega = \sqrt{2}\pi/a_0\omega_0$ and its proper angular frequency ω thus depends linearly on a_0. This means the higher the laser amplitude, the faster the pendulum oscillations. Note also that only when $a_0 = 1/\sqrt{2}$ does the pendulum oscillate at the laser frequency ($\omega = \omega_0$).

Even in the relativistic regime, the system is again fully integrable in the Liouville sense, as we find a third motion invariant, which is simply γ:

$$mc\frac{d\gamma}{dt} = \frac{e^2}{2\gamma mc}\frac{\partial A^2}{\partial t} = \frac{e^2}{2\gamma mc}\frac{\partial}{\partial t}(1+\cos(2k_0x)) = 0. \tag{22}$$

This shows that in this configuration, p_x and $\boldsymbol{p}_\perp$ still evolve in time, but the total kinetic energy remains constant. The electron motion is predictable and does not exhibit any chaotic behavior.

2. *Equations of motion in colliding linearly polarized waves*

This time, both laser waves have a linear polarization along the same direction, e.g., z. In the following, we refer to this configuration as L/L. For two counterpropagating waves, the transverse vector potential $\boldsymbol{A}$ for each wave reads

$$\boldsymbol{A}_1 = A_0\sin(\omega_0 t - k_0 x)\boldsymbol{z},$$
$$\boldsymbol{A}_2 = A_0\sin(\omega_0 t + k_0 x)\boldsymbol{z}, \tag{23}$$

and the spatial partial derivative of A^2 is

$$\frac{\partial A^2}{\partial x} = A_0^2\frac{\partial}{\partial x}([\sin(\omega_0 t - k_0 x) + \sin(\omega_0 t + k_0 x)]^2) = -2A_0^2 k_0\sin(2k_0x)(1-\cos(2\omega_0 t)). \tag{24}$$

The equation of motion becomes

$$\frac{d^2x}{dt^2} - a_0^2c^2k_0\sin(2k_0x)[1-\cos(2\omega_0 t)] = 0. \tag{25}$$

Again, using $\pi + 2k_0x \to \theta$ and $t + \pi/2\omega_0 \to t'$, we get

$$\frac{d^2\theta}{dt'^2} + \underbrace{2\,a_0^2\,\omega_0^2}_{\omega^2}\sin\theta(1+\cos(2\omega_0 t')) = 0. \tag{26}$$

In the following, we use t instead of t' for the sake of clarity.

This equation is the one of a forced pendulum commonly known as *Kapitza's pendulum* [14,15]: this is a rigid gravity pendulum in which the pivot point (also known as the attached point) is forced to quiver in the vertical direction, up and down. In the nonrelativistic limit, the motion of an electron in two colliding linearly polarized waves is thus analogous to a forced pendulum, which is known to behave chaotically for some parameters of the driving force (amplitude, frequency) [16].

In Fig. 2, we summarize the various configurations of laser wave polarization discussed in this section. Based on the inherent forms of the pendulum equations, this makes it easy to discriminate which configuration can potentially lead to chaotic dynamics, and which cannot. So far, we saw that only the configuration involving two colliding linearly polarized waves has the potential for a chaotic behavior. Note, however, that this is only the case when the two waves are exactly counterpropagating. If the angle between the two waves is different from 180°, then chaos can also develop for other polarization configurations (see Sec. V).

C. Numerical analysis of electron dynamics in two colliding waves

At this point, one cannot go any further in the analytical analysis of the forced pendulum equations without a heavy formalism. We therefore turn to numerical "particle-tracking" (PT) simulations that solve equations of motion for a given initial distribution of test particles in a known EM field. Unlike the kinetic particle-in-cell method [17,18], PT simulations solve equations of motion independently for each electron, without including any mutual interactions.

This subsection aims at getting the physical insight required to develop the model described in Sec. III, and identifying the physical representations that will be essential to understand the remainder of this work. In this regard, we will use PT simulation results to analyze the two main configurations of interest: RHC/LHC and L/L.

In all PT simulations, 10^5 noninteracting "test" electrons are initially located along the x-axis in the range $[-\lambda_0, \lambda_0]$, with random initial positions and zero longitudinal momentum ($p_{x|_{t=0}} = 0$). The EM waves are considered infinite in time and space, which imposes that all particles are directly initialized within the interference field. To ensure that the particles also have zero transverse momentum in the absence of the EM field, the momentum needs to be initialized to the transverse vector potential corresponding to the particle's initial position: $\boldsymbol{p}_{\perp|_{t=0}}(\mathrm{x}) = e\boldsymbol{A}_{|_{t=0}}(\mathrm{x})$ [Eq. (5)].

1. *Dynamics in two colliding circularly polarized waves*

The superposition of RHC- and LHC-polarized plane waves defined in Eq. (17) leads to the following interference field:

$$\boldsymbol{E} = +\sqrt{2}\,E_0\cos(k_0x)(\sin(\omega_0 t)\,\boldsymbol{y} - \cos(\omega_0 t)\,\boldsymbol{z}),$$
$$\boldsymbol{B} = -\sqrt{2}\,B_0\sin(k_0x)(\sin(\omega_0 t)\,\boldsymbol{y} - \cos(\omega_0 t)\,\boldsymbol{z}). \tag{27}$$

Snapshots of this interference field are displayed in Fig. 3(a) as a function of x at different times within a laser

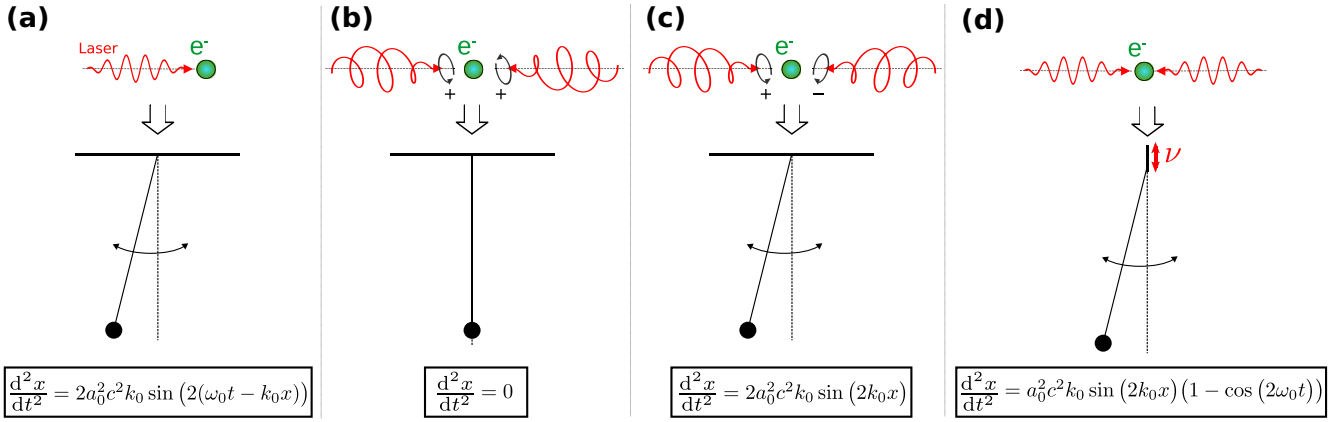

FIG. 2. Formal analogy between a pendulum and the dynamics of an electron in two colliding waves. Each panel presents a different interaction configuration: (a) interaction of an electron with only one linearly polarized wave, (b) with two RHC circularly polarized waves, (c) with one RHC- and one LHC-polarized wave, and (d) with two linearly polarized waves. For each case, we remind the reader of its equivalent pendulum: (a) and (c) simple gravity pendulum, (b) pendulum *at rest*, and (d) Kapitza pendulum.

period (see the plain, dashed, and dotted lines). It forms a standing wave, with the electric field nodes located at $k_0x = \pi/2 + n\pi$ ($\forall n \in \mathbb{Z}$) and the magnetic field nodes at $k_0x = n\pi$. These magnetic nodes will play a key role in our subsequent analysis.

The electron distribution in the (x, p_x) phase space after two laser periods in this field is pictured in Fig. 3 when using the nonrelativistic [Fig. 3(b)] and relativistic [Fig. 3(c)] equations of motion in the PT simulations. In the remainder of this article, the color scale of particle markers in phase space is related to the electron initial position $x_{|_{t=0}}$. It is coded as a set of four different colors, each corresponding to a different *magnetic field bucket*, defined as the area between two magnetic field nodes and delimited by vertical black dashed lines. Each bucket is centered around an electric field node. From the different profiles of Figs. 3(b) and 3(c), one can infer three important observations:

(i) The distributions look like simple pendulum phase portraits, where all the trajectories are trapped. The particles are simply rotating around fixed points on a close elliptical orbit. These fixed points coincide exactly with electric field nodes.

(ii) The particle colors do not mix, implying that particles are staying in their initial bucket all along the interaction.

(iii) There is almost no difference between nonrelativistic and relativistic regimes except for the slight change of amplitudes of the inner ellipses.

As stated in the previous subsection, the electron dynamics in counterpropagating circularly polarized waves can be analyzed as a simple pendulum dynamics. Numerical simulations confirm that particle dynamics is not chaotic in this case.

2. *Dynamics in two linearly polarized waves*

We showed that when the laser wave polarizations are switched from circular to linear, the equation of motion of particles is identical to that of a Kapitza's pendulum, which is known to no longer be predictable when the driving force becomes large enough. In appropriate conditions (namely, for large enough laser fields), we should thus expect some clear signatures of chaos when looking at the particle distribution in phase space.

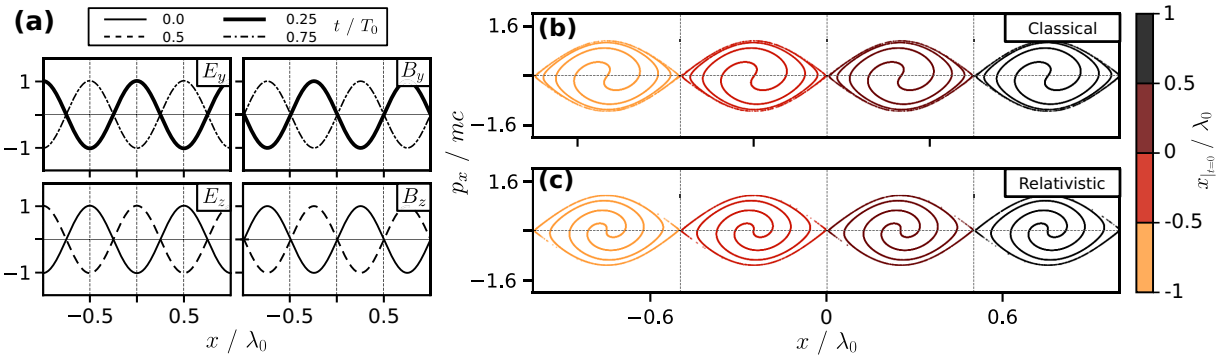

FIG. 3. Electron dynamics in RHC/LHC configuration. Panel (a) shows the field resulting from the interference of counterpropagating RHC-polarized and LHC-polarized waves. Each line style corresponds to a different time within a laser period. In addition, the positions of magnetic field nodes are highlighted by vertical dashed lines. In panels (b) and (c), we represent the electron distributions in phase space after $2T_0$ in the fields of panel (a) for $a_0 = 0.8$, when using the nonrelativistic (b) and relativistic (c) forms of the equations of motion. The discrete color scale (right) encodes the different buckets in which particles were initially located.

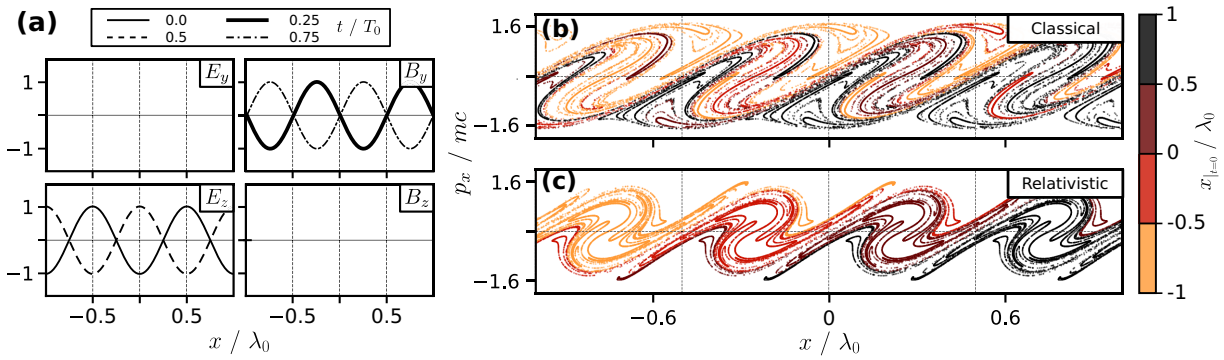

FIG. 4. Electron dynamics in L/L configuration. Similar to Fig. 3 but for two linearly polarized lasers.

In this configuration, the interference field reads

$$\boldsymbol{E} = -2\,E_0\cos(k_0x)\cos(\omega_0t)\,\boldsymbol{z},$$
$$\boldsymbol{B} = +2\,B_0\sin(k_0x)\sin(\omega_0t)\,\boldsymbol{y}. \tag{28}$$

This field is displayed in Fig. 4(a). Again, the electric field nodes are located at $k_0x = \pi/2 + n\pi$ $(\forall n \in \mathbb{Z})$ and the magnetic field nodes are at $k_0x = n\pi$. In this configuration, the magnetic and electric fields oscillate in quadrature, both in space and time.

The electron phase space distributions calculated in this interference field are pictured in Figs. 4(b) and 4(c) at $t = 2\,T_0$. We have performed the same PT simulation as in the RHC/LHC case, with both the nonrelativistic and relativistic equations of motion. The particle distributions present striking differences from the ones obtained in the previous case:

(i) First, the particles can now migrate between buckets. This is indicated by the fact that the "particle colors" are getting all mixed up as time evolves.

(ii) The magnitude of the particle momentum is higher than in the RHC/LHC configuration.

(iii) The general form of the relativistic and nonrelativistic distributions of Figs. 4(b) and 4(c) is extremely different from that observed in the RHC/LHC configuration, and is characterized by a complex multilayered structure, especially near the magnetic field nodes (interface of the buckets).

Similarly to the circular polarization, the electric field nodes keep behaving as fixed points around which the whole particle distribution is rolling in phase space. In the following, we explain how the observed multilayer structure originates from a periodic *stretching and folding* of the phase-space distribution around these fixed points, and the key role of this effect in the emergence of chaos.

IV. MODEL FOR STRETCHING AND FOLDING IN TWO WAVES

A. Stretching and folding: A two-step mechanism leading to chaos

Stretching and folding refers to a two-step evolution in phase space that can often lead to chaotic dynamics: the stretching phase results in nearby points in phase space diverging, and the folding phase results in distant points being mixed together. This is actually very similar to a common culinary operation, i.e., when one wants to quickly distribute ingredients into a solid dough or introduce a multilayer structure. A famous example is the puff pastry, a French dough presenting dozens of thin layers obtained by rolling out and folding a regular dough with fat. For a salted dough, it is possible to drop a single pinch of salt on top before starting the process. Then, the salt will diffuse and be equally distributed inside the pastry after only a few stretching and folding steps. This can be viewed as a consequence of a chaotic dynamics within the dough, leading to an exponential divergence of the positions of initially neighboring salt grains (positive Lyapunov exponent).

In this section, we explain how the time evolution of the ponderomotive force results in a stretching and folding effect on the phase-space distribution of electrons in two counterpropagating linearly polarized EM waves (L/L configuration), thus leading to chaotic dynamics. But we first briefly analyze the rather trivial dynamics in the RHC/LHC configuration: although chaotic dynamics does not arise in this case, it will turn out to be very helpful to understand the more complex L/L configuration.

1. Electron dynamics in the RHC/LHC configuration

As a reminder, the electron dynamics in the RHC/LHC case is governed by the following ponderomotive force in the nonrelativistic regime (see Sec. III):

$$-\partial_x A^2 = 2\,A_0^2k_0\,\sin(2k_0x). \tag{29}$$

It turns out that even if both the **E** and **B** fields depend on time, the ponderomotive force (right-hand side), which results from the combined effects of all fields, is independent of time and only varies spatially along the longitudinal direction. A free electron placed in this field is thus exposed to a static potential, which is sinusoidal in space. This results in a very simple dynamic, summarized below.

In Fig. 5, we plot the evolution of the electron distribution in colliding circularly polarized lasers ($a_0 = 3$) at different times within half a laser period. The plots are zoomed on a single magnetic bucket. A typical particle orbit is highlighted in red and follows a trajectory on a closed orbit, similarly to a simple gravity pendulum. Using the coordinate $\theta = \pi + 2k_0x$ introduced earlier, the velocity $v_\theta = d\theta/dt$ along this orbit

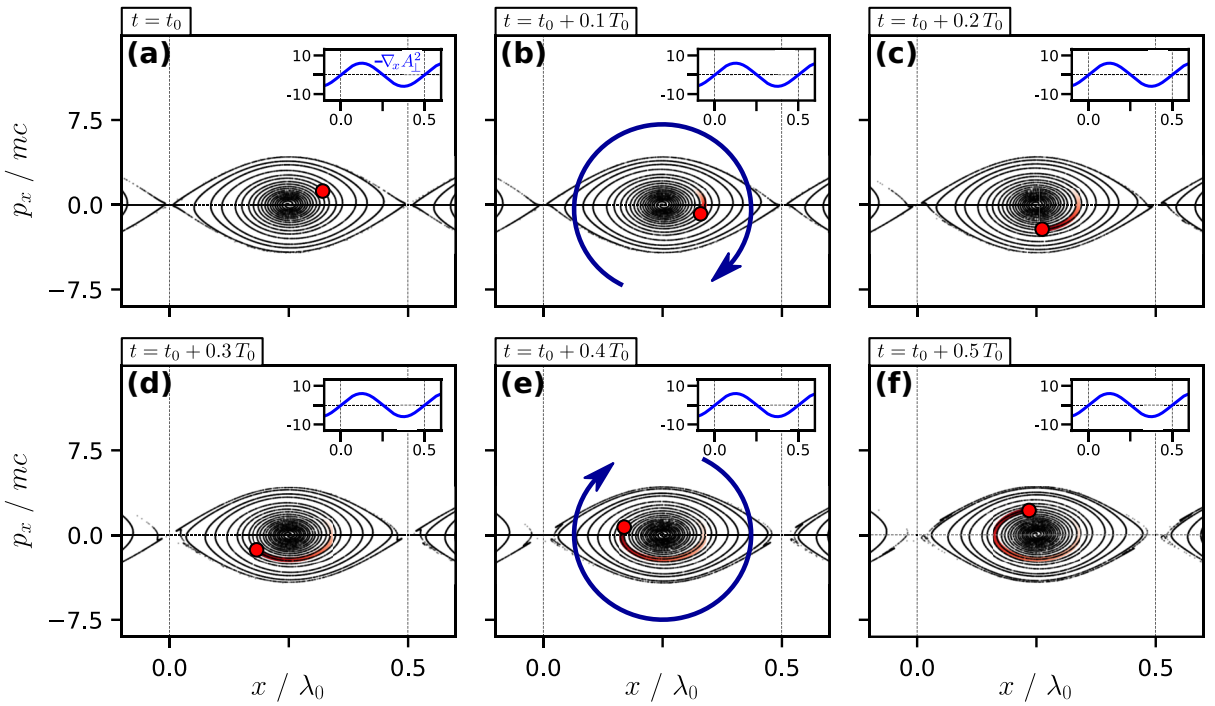

FIG. 5. Temporal evolution of the electron phase-space distribution in the RHC/LHC case. This figure illustrates different snapshots of the electron distribution in phase space at different times labeled on top of each panel. Here, the laser intensity is $a_0 = 3$. A typical particle is highlighted as a large red dot and its trajectory as the red trail. In the top-right corner of each panel, we plot the spatial profile of the ponderomotive force, which is independent of time in this field configuration.

can be calculated as follows in the nonrelativistic regime:

$$\frac{d^2\theta}{dt^2} = -2\,a_0^2\,\omega_0^2\,\sin\theta \tag{30}$$

$$\Rightarrow \frac{1}{2}\left(\frac{d\theta}{dt}\right)^2 = 2\,a_0^2\,\omega_0^2\,\cos\theta + C^{\rm st}$$

$$\Rightarrow v_\theta^2 = 4\,a_0^2\,\omega_0^2\,(\cos\theta - \cos\theta_0) \tag{31}$$

with θ_0 the initial electron position. For small θ, Eq. (30) reduces to the equation of a harmonic oscillator, and the trajectories close to the electric nodes (such as the one of the red particle) are elliptical. The orbit defined with $\theta_0 = \pi$ delimits trapped and circulating particles and is called the separatrix. For a population initially at rest, one can note that all particles are located below the separatrix and hence follow closed orbits.

2. *Stretching and folding in the L/L configuration*

As a reminder, the electron dynamics in the L/L case is governed by the following ponderomotive force in the nonrelativistic regime (see Sec. III):

$$-\partial_x A^2 = 2\,A_0^2 k_0\,\sin(2k_0x)(1 - \cos(2\omega_0 t)). \tag{32}$$

This force has the same spatial dependence as in the RHC/LHC configuration, but the amplitude of the spatially sinusoidal force is now oscillating in time. A key point is that the temporal term $(1 - \cos(2\omega_0 t))$ is always positive, so that the sign of the force is determined by the sign of $\sin(2k_0x)$. This means that as in the RHC/LHC case, this force will always be positive on the left part of an electric field node (e.g., $x \leqslant 0.25\,\lambda_0$), and negative on the right part ($x \geqslant 0.25\,\lambda_0$). The consequence is that electrons are always attracted toward electric field nodes even in the L/L case. In other words, the potential experienced by the electron is the same as in the RHC/LHC case, but *its amplitude is now modulated in time.*

To understand how this temporal modulation considerably modifies the electron dynamics compared to the RHC/LHC case, we will now decompose this dynamics in two main temporal phases, periodically repeated every half optical period of the laser field, and which can be clearly identified in Fig. 6:

(i) $\mathbf{t_0 \leqslant t \leqslant t_0 + 0.25\,T_0}$ [Figs. 6(a)–6(c)]: the ponderomotive force is off and stays close to zero, allowing the particles to remain free from any force. The particles thus follow a ballistic motion, illustrated by the blue arrows in Fig. 6(b): all particles located in the upper part of the plot ($p_x > 0$) are traveling towards positive x at constant velocity. Similarly, particles located in the lower part of the plot ($p_x < 0$) are traveling towards negative x. The trajectory of the red particle in Fig. 6(c) is almost straight and horizontal. During this phase, the full phase-space distribution gets elongated along the x-axis: this is the *stretching phase*.

(ii) $\mathbf{t_0 + 0.25\,T_0 \leqslant t \leqslant t_0 + 0.5\,T_0}$ [Figs. 6(d)–6(f)]: the ponderomotive force turns on again, and is similar to the one obtained in the RHC/LHC case. The electron motion is similar to Fig. 5, for which the particles were rotating around the electric field node. The rotation is illustrated with the blue curved arrow in Fig. 6(e). This arrow always points in a clockwise direction because the ponderomotive force keeps the same sign on both sides of an electric node over time. The red trajectory follows a circular arc between Figs. 6(d)

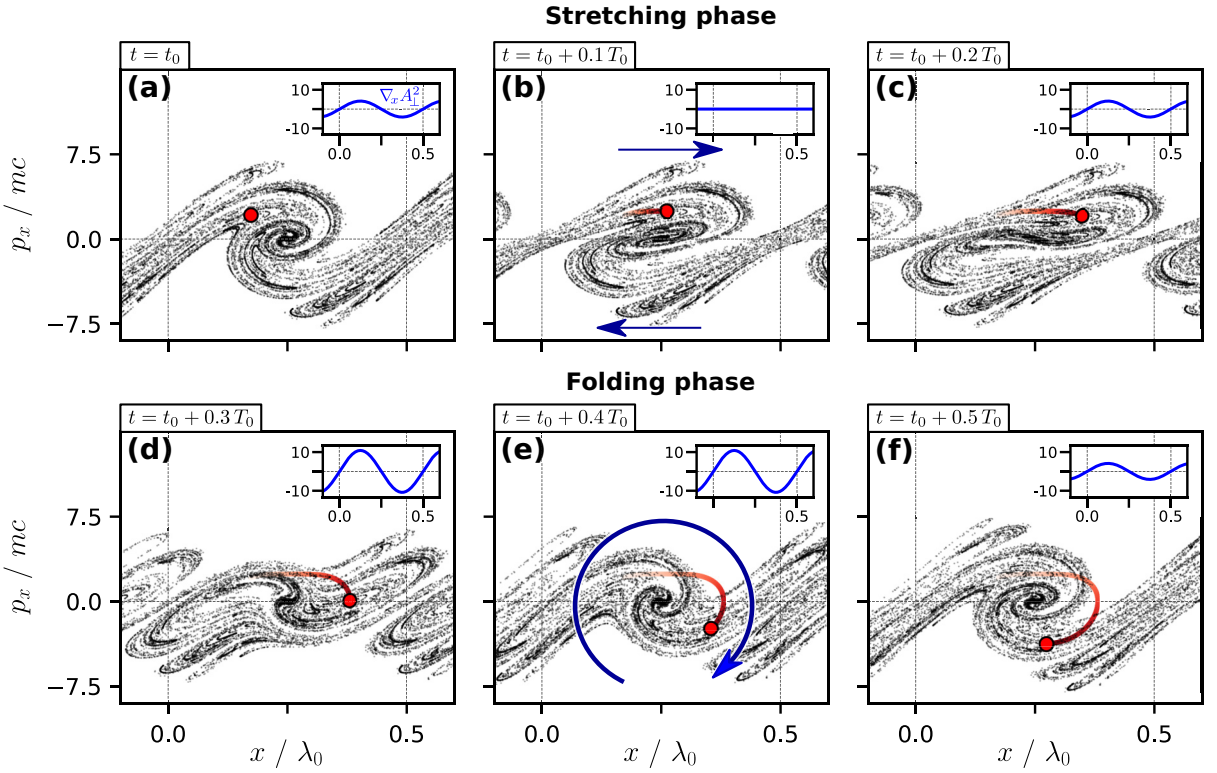

FIG. 6. Temporal evolution of the distribution of electrons in the L/L case. Same as Fig. 5 now for two linearly polarized waves. The ponderomotive force now evolves in time, and the evolution of the phase-space distribution is characterized by two distinct steps: (a)–(c) stretching phase, with a horizontal elongation illustrated by two blue arrows, and (d)–(f) folding phase, with a rotation around an electric field node illustrated by the curved blue arrow.

and 6(f). The full distribution rotates around the electric field node: this is the *folding phase*.

3. Reduced model of stretching and folding

The transition from one phase to the next is a smooth and continuous one since the ponderomotive force varies as a cosine. To develop a simple model, we approximate this temporal evolution by a piecewise signal, thus clearly dissociating the stretching from the folding. The temporal term is now a piecewise function that periodically switches from 0 to 2 and vice versa [19] with a period of $T_0/2$:

$$-\partial_x A^2 \sim \begin{cases} 0, & n < \frac{2t}{T_0} < n + \frac{1}{2}, \\ 4A_0^2 k_0 \sin(2k_0 x), & n + \frac{1}{2} < \frac{2t}{T_0} < n + 1, \end{cases} \tag{33}$$

with $n \in \mathbb{Z}$. This type of approximation is similar to the one used to solve nonlinear Meissner's equations [20–23]. This simplified case is interesting because the equation of motion is solvable analytically on both time intervals. This will be important in the following sections for deriving analytical models of key features of stochastic heating.

Under this approximation, it instantly turns out that over half a laser period the particles follow a ballistic motion for $t \in [0,\ T_0/4]$ and a simple pendulum-type motion for $t \in [T_0/4,\ T_0/2]$ [same form as the RHC/LHC case in Eq. (29)]. The temporal evolution of the phase-space distribution obtained from numerical simulations with this simplified model is displayed in Fig. 7. The red electron trajectory exhibits a clear transition from a ballistic motion at constant p_x [Figs. 7(a)–7(c)] to an elliptical motion [Figs. 7(d)–7(f)]. The electron distribution resembles the one given by Fig. 6, even though the approximation of approaching the sinusoidal temporal term by a step function might appear rough.

B. Transition to chaos: Criterion for chaos threshold

We now show how the analysis of the stretching and folding mechanism presented in the previous subsection and the corresponding model allow us to derive a simple criterion for the onset of chaos.

Before starting this derivation, it is useful to briefly return to the analogy with the mechanical pendulum. For such a pendulum, there are two special positions of the bob: the bottom stable position and the top unstable position, respectively called the O point and the X point in the following [Fig. 8(a)]. The dynamical properties around the X point are particularly important: when the bob is located at this point, it can drop either towards the left or towards the right, depending on its *exact* velocity at that moment. Small discrepancies on the bob velocity at this point can thus lead to two very different trajectories: one where the bob fails to cross the X point and thus turns back, and one where it does cross the X point and keeps going the same way. As a result, very small changes on the initial velocity can lead to totally different bob trajectories. This sensitivity to initial conditions is the seed that can in some conditions lead to chaotic dynamics.

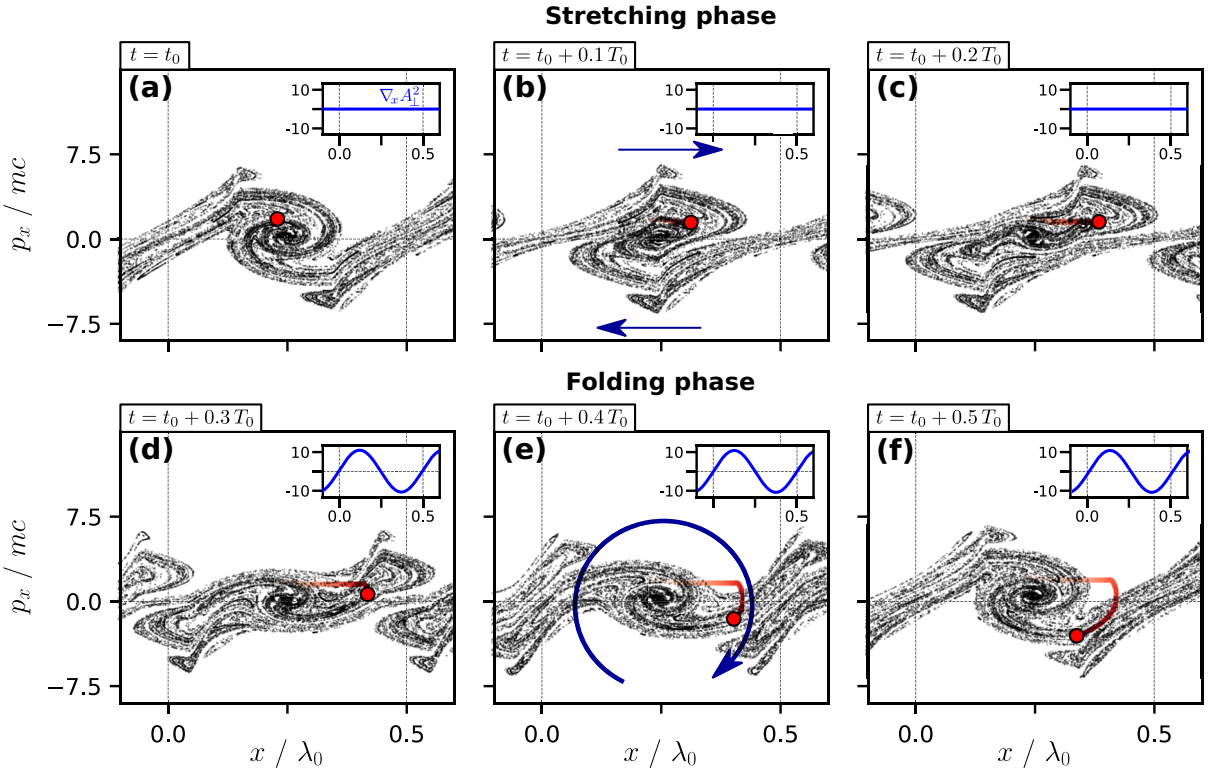

FIG. 7. Temporal evolution of the distribution of electrons in the simplified ***L*/*L*** case. Same as Figs. 5 and 6 but when the ponderomotive force is modeled by a constant piecewise function defined by Eq. (33), in order to clearly separate the two different phases of the electron dynamics.

Such chaotic dynamics is known to be possible for a forced pendulum. Each time the bob approaches the X point, some neighboring trajectories diverge rapidly. For a strong enough driving force, the crossing of the X point is repeated a large number of times, and two trajectories, even very close initially, will end up diverging at an exponential rate. This is one of the main criteria to define a chaotic dynamic.

Let us now exploit this simple idea to understand the origin of chaos in the dynamics of an electron in counterpropagating waves. According to the analysis of Sec. III, in the interference field of the two EM waves, the electric field nodes actually play the role of O points, while the magnetic field nodes play the role of X points [Fig. 8(b)]. For field configurations where the particle is forced to cross the unstable X points multiple times, it will sometimes succeed in crossing the X point, and sometimes not: this leads to a random diffusion of the particle between magnetic buckets, and potentially to chaotic dynamics.

This diffusion is not possible in the RHC/LHC configuration: the particle travels along close orbits within a single

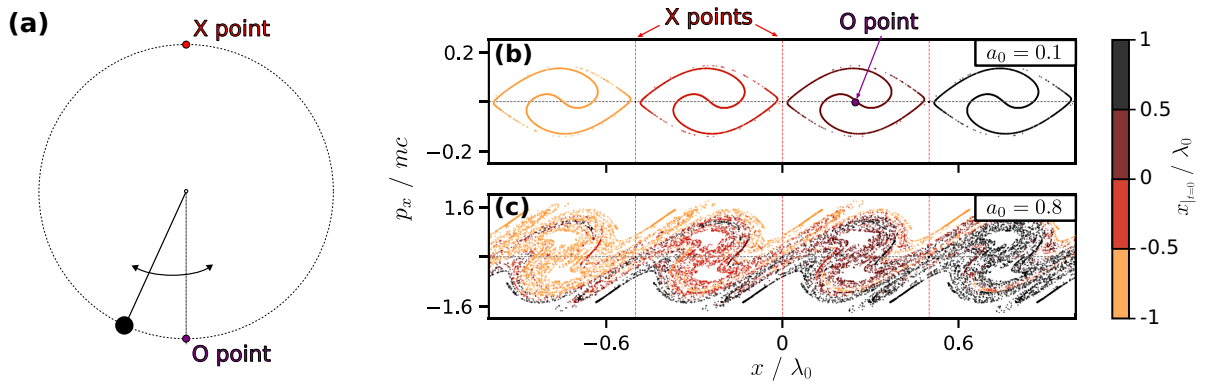

FIG. 8. Analogy between the dynamics of a pendulum and of an electron in two EM waves. Panel (a) shows a sketch of a forced pendulum highlighting the two points of interest: the unstable X point and the stable O point. In panels (b) and (c), we represent the distribution of electrons in phase space after four laser periods ($4\,T_0$) for two linearly polarized lasers [full relativistic model without approximation, cf. Eq. (10)], below [$a_0 = 0.1$, panel (b)] and beyond [$a_0 = 0.8$, panel (c)] the chaos threshold. The equivalents of the O and X points are shown for this configuration.

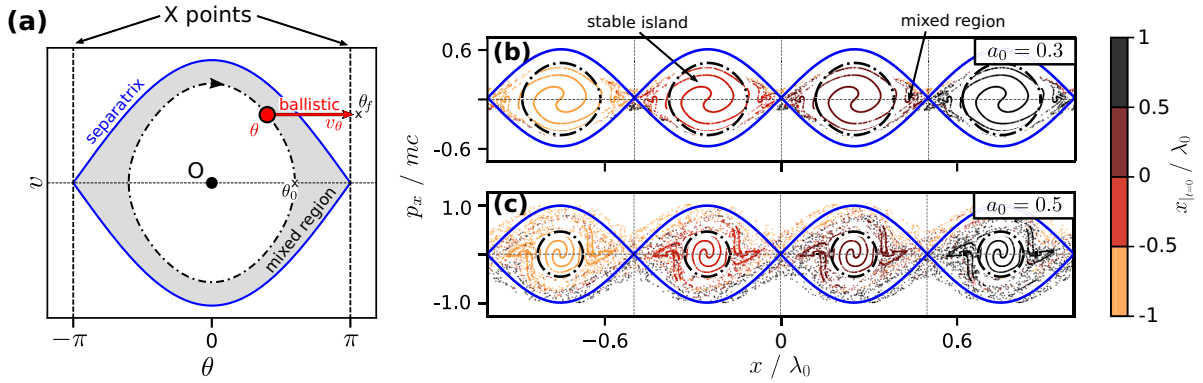

FIG. 9. Electron dynamics in the L/L case in the transition regime from nonchaotic to fully chaotic dynamics. In panel (a), a particle (in red) on a trapped orbit during the folding phase (black dot-dashed line) then follows a ballistic motion from (θ_i, v_{θ_i}) to (θ_f, v_{θ_i}) during the stretching phase. If it is fast enough and/or sufficiently close to the separatrix, it can cross an X point along the way and thus move to a neighboring bucket. This is possible for particles within the gray area, called the mixed region. In panels (b) and (c), we represent the distribution of electrons in phase space after $4T_0$ for two linearly polarized lasers [fully relativistic model without approximation; cf. Eq. (10)]: (b) $a_0 = 0.3$ and (c) $a_0 = 0.5$. The blue envelope is the separatrix. The black dot-dashed lines show the limit orbit that separates the distribution into two areas: a stable island and a mixed region. It has been obtained with the analytical model presented in the text.

bucket, trapped by the constant potential well formed by the two EM waves. The situation radically changes in the L/L configuration. The key difference is that the potential periodically switches off, during what we have called the stretching phases: the particle then temporarily follows a ballistic motion, characterized by a constant velocity. If the particle is fast enough during this phase, it can possibly cross an X point, and thus penetrate into the neighboring bucket before the next folding phase starts.

This analysis shows that the key parameter determining the nature of the particle dynamics is $v_{\theta_i} = d\theta/dt(t = t_i)$, the velocity at the time t_i corresponding to the end of the folding phase and the beginning of the stretching phase. The typical magnitude of this velocity is determined by the amplitude of the EM waves. If this amplitude is low, most particles are too slow to leave their bucket, and the distribution in phase space looks like the stable RHC/LHC case. This regime is illustrated in Fig. 8(b). In contrast, for a high enough wave amplitude, the particle can cross the X point and explore many different buckets over time, leading to particle diffusion and chaotic dynamic. This regime is illustrated in Fig. 8(c). The diffusion of particles across multiple buckets leads to the "color mixing" in phase space already emphasized in Fig. 4.

We now analyze the dynamics of the system in between the two limit regimes of Figs. 8(b) and 8(c) to determine the threshold on the EM wave amplitude for the emergence of chaotic dynamics. Our analysis is guided by the results of numerical simulations, illustrated in Fig. 9. As a_0 is increased, the bounded periodic orbits of Fig. 8(b)—corresponding to the "stable area" located below the separatrix—gradually become unbounded and chaotic within a part of the phase space which we call *the mixed area*, highlighted in gray in Fig. 9(a). This name refers to the fact that within each period, some particles in this area remain inside a fixed bucket while some others escape to a neighboring one.

As a_0 gets larger, this mixed area gradually expands from the separatrix down to the O point, while the stable area correspondingly shrinks towards the O point—a limit corresponding to the fully developed chaotic regime. Conversely, when a_0 is decreased, the mixed area eventually totally vanishes: the amplitude $a_0 = a_0^T$ where this occurs corresponds to the threshold for the onset of chaos. The transition regime between this onset of chaos and fully developed chaos is illustrated in Figs. 9(b) and 9(c), which display typical phase-space distributions for $a_0 = 0.3$ and 0.5. The shrinking of the stable area and the expansion of the mixed region, as a_0 increases, are clearly observed between these two panels.

We now derive an analytical model for the extent of the mixed region. To do so, we consider the simplified form of the stretching and folding mechanism defined in Eq. (33), and we define $\theta = \pi + 2k_0 x$ as before. Here, we use the nonrelativistic form of the equations of motion as we only consider a range of laser amplitudes $0.1 < a_0 < 0.8$ encompassing the chaos threshold and for which relativistic effects do not play a major role. Using the reduced model of stretching and folding, the nonrelativistic equations of motion read

$$\begin{aligned} &\frac{d^2\theta}{dt^2} + 4\,a_0^2\,\sin\theta = 0 \quad \text{for folding,} \\ &\frac{d^2\theta}{dt^2} = 0 \qquad \text{for stretching.} \end{aligned} \tag{34}$$

During the folding phase, particles are rotating around an electric field node along closed orbits. We parametrize these closed orbits using θ_0, the position of the particle when it has zero velocity. The orbit corresponding to a given θ_0 is pictured as a black dotted-dashed line in Fig. 9(a). According to Eq. (31), along the particle orbit, θ and v_θ are bound by the following formula:

$$v_\theta = 2\sqrt{2}a_0\omega_0\sqrt{\cos\theta - \cos\theta_0}. \tag{35}$$

At the end of the folding step, a particle on this orbit is located at a position (θ_i, v_{θ_i}) in phase space [displayed in red in Fig. 9(a)]. During the subsequent stretching phase, the velocity v_{θ_i} then remains constant, and this phase lasts for a time interval of half a laser period $T_0/2$, i.e., π/ω_0. When the ballistic motion ends, a new point (θ_f, v_{θ_i}) in phase space has been reached, with θ_f the position at the end of the stretching

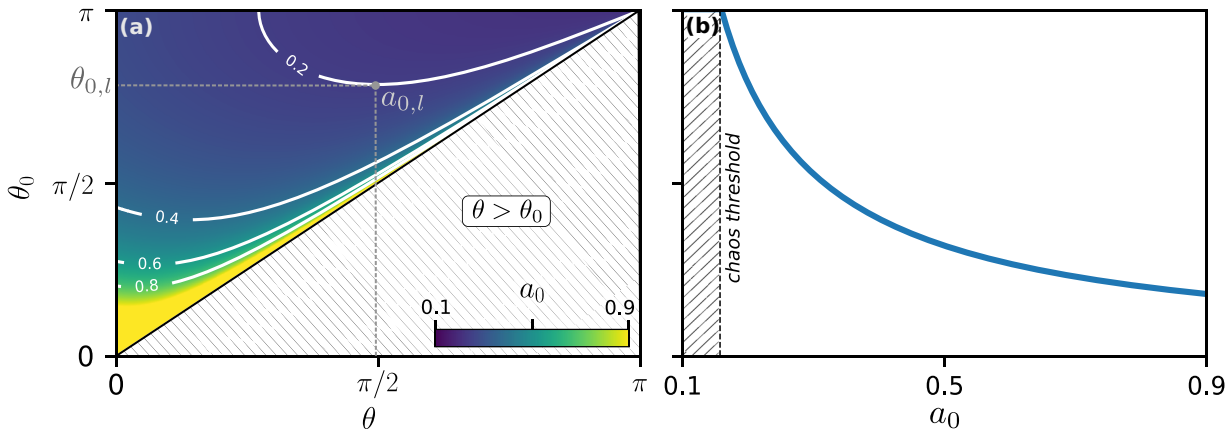

FIG. 10. Derivation of the chaos threshold. In panel (a), the minimum laser wave amplitude a_0^m required for a particle to move to a neighboring bucket is plotted in color code, as a function of θ_i and θ_0 [Eq. (37)]. θ_i is always smaller than θ_0, so that the bottom-right part is forbidden. In addition to the color scale, we plot as plain white lines different isocontours corresponding to $a_0 = 0.2,\ 0.4,\ 0.6,\ 0.8$. For a given amplitude (e.g., $a_0 = 0.2$), the parameter $\theta_{0,l}$ of the limit orbit between the stable and mixed areas is obtained by minimizing θ_0 along the a_0 isocontour. The resulting $\theta_{0,l}$ is plotted as a function of a_0 in panel (b). $\theta_{0,l}$ tends to π as a_0 decreases, and is no longer defined below the chaos threshold ($a_0^T \sim 0.159$).

phase. A particle has escaped its initial bucket if θ_f lies beyond the X point, i.e., if $\theta_f > \pi$ [see Fig. 9(a)]. This reads

$$\theta_f = \theta_i + \pi/\omega_0 \times v_{\theta_i} > \pi. \tag{36}$$

Replacing v_{θ_i} by its value yields the condition

$$a_0 > a_0^m = \frac{\pi - \theta_i}{2\sqrt{2}\pi\sqrt{\cos\theta_i - \cos\theta_0}}. \tag{37}$$

In Fig. 10(a), this minimum wave amplitude a_0^m required to fulfill the condition of Eq. (36) is plotted in color code in the (θ_i, θ_0) space. The whole bottom-right part of the figure is forbidden since $\theta_i \leqslant \theta_0$ by definition of the orbit and of θ_0.

For a fixed wave amplitude a_0, an orbit is located within the mixed region of the phase space if it exists some positions θ_i which allow the particle to leave its buckets. Determining the border of this mixed region means determining the parameter $\theta_0 = \theta_{0,l}$ of the limit orbit along which *one value only* of θ_i fulfills this condition. This critical value $\theta_{0,l}$ can be found graphically using Fig. 9(a). To this end, we plot a_0-isocontours on this color map as white lines [see Fig. 9(a)]. For a given laser wave amplitude a_0, $\theta_{0,l}(a_0)$ is the value of θ_0 at the minimum of the corresponding isocontour. For example, in Fig. 10(a) we highlight the value $\theta_{0,l}$ corresponding to $a_0 = 0.2$ using dotted lines. This defines the limit orbit between the stable and mixed areas for this wave amplitude. In Figs. 9(b) and 9(c), two examples of limit orbits found in this way, for two wave amplitudes, are pictured as a black dotted-dashed line, and nicely match the limit between chaotic and nonchaotic areas observed in PT simulations.

Using this analysis, we can determine the limiting orbit between the stable and mixed regions as a function of the wave amplitude a_0 by calculating $\theta_{0,l} = f(a_0)$. This function is plotted in Fig. 10(b). As a_0 decreases, $\theta_{0,l}$ tends to π, i.e., the limiting orbit tends to the separatrix. $\theta_{0,l}$ is no longer defined below a certain amplitude: this is the threshold for the onset of chaos, a_0^T. For amplitudes below this value, none of the particles are diffusing between neighboring buckets, even those exactly located on the separatrix. Since the separatrix corresponds to $\theta_0 = \pi$, this implies that a_0^T has to fulfill

$$a_0^T < \frac{\pi - \theta_i}{2\sqrt{2}\pi\sqrt{\cos\theta_i + 1}}. \tag{38}$$

The right-hand-side quantity is minimal when $\theta_i \to \pi$. Using a Taylor expansion of the cosine function to calculate its limit for $\theta_i \to \pi$, we conclude that the mixed area starts developing as soon as

$$a_0 > a_0^T = \frac{1}{2\pi} \simeq 0.159. \tag{39}$$

This simple physical approach thus provides a value for the threshold on the EM waves amplitude for chaos development, but it also provides an intuitive understanding of its physical meaning. This threshold value a_0^T is very close to the results obtained in the literature through numerical simulations or by much more formal theoretical analysis [2,3].

V. RANDOM WALK MODEL

In this section, we consider wave amplitudes well above the chaos threshold, i.e., $a_0 \gg a_0^T$. Beyond this threshold, particles explore many different buckets, sometimes far from their initial position. This diffusion process is akin to a random walk, where the issue of each random sampling is "remain in" or "escape from" their current bucket. This random sampling is performed with a period corresponding to the stretching and folding period $T_0/2$. Indeed, at each stretching and folding period, particles in the mixed region will reach an X point and then either leave or remain in their initial bucket, while particles in stable islands never leave their buckets. In the

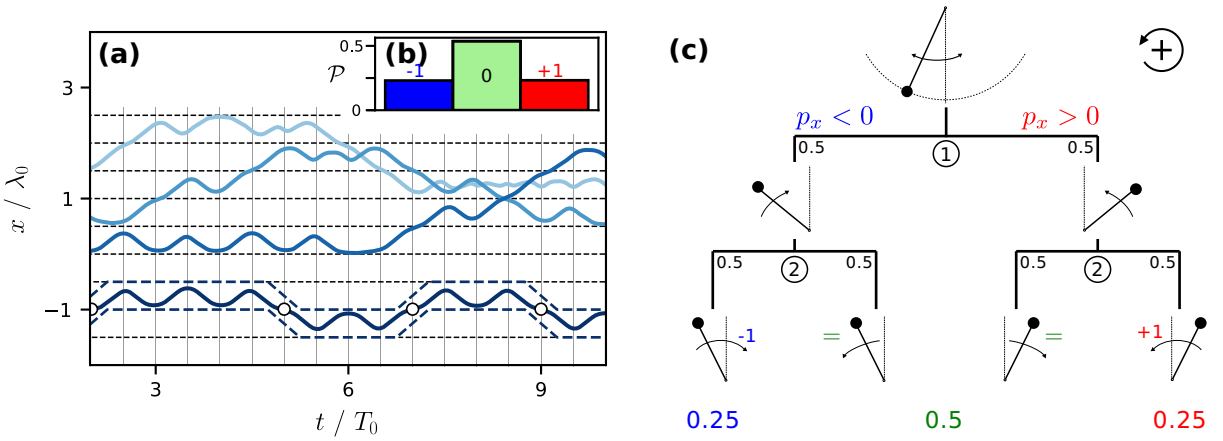

FIG. 11. Particle trajectories as a random walk. In panel (a), four particle trajectories are plotted with different shades of blue. The magnetic nodes are drawn as black dashed lines. For the bottom dark blue trajectory, we highlight its current buckets (dark blue dashed line) as well as the positions and times at which jumps from one bucket to another occur (white dots). At the end of every $T_0/2$ period, a particle can either cross a boundary and then change bucket (events ± 1) or stay in its bucket (event 0). We report in panel (b) the proportions of the three different outcomes summed over a whole simulation for 10^5 particles and $a_0 = 3$. Finally, panel (c) displays the probability tree discussed in the text, illustrated with the pendulum analogy.

relativistic limit ($a_0 \geqslant 1 \gg a_0^T$), the mixed region essentially covers the full bucket. As all particles travel at the same speed $\approx c$ and as a bucket width is exactly $cT_0/2$, they will all reach an X point, and thus undergo a random sampling every $T_0/2$.

To illustrate this random walk process, some typical particle trajectories are plotted in Fig. 11(a) in the case of two counterpropagating linearly polarized waves with $a_0 = 3$. All particles start at $x = 0$ at $t = 0$. As before, the magnetic nodes are emphasized by black dashed lines. Particles are observed to jump from one bucket to another in a random fashion. As expected, particles come close to an X point each $T_0/2$ and can only jump between buckets at these specific times (light gray vertical lines).

Let us now focus on the bottom dark blue trajectory, for which we highlight both the boundaries of the two surrounding buckets (thick dark blue dashed lines) and the jumps between buckets (white dots). At each $T_0/2$, this particle gets close to a bucket boundary and either leaves or remains in its current bucket. The particle behavior appears to be totally random, i.e., nothing *seems* to determine *a priori* if the particle will leave the bucket or not. The crossing of a boundary by the particle is thus analogous to a Bernoulli trial, where a fair coin is tossed at every multiple of $T_0/2$: *heads* would be a leave and *tails* would be a stay. Both of these events end up being equiprobable. In this section, we use this idea to determine an equation for the position and energy distributions of particles.

A. Probabilistic model

Exploiting yet again the pendulum analogy, we sketch a probability tree in Fig. 11(c) to determine the probability law of outcome associated with each "coin toss" event. A "coin toss" event occurs for each particle every $T_0/2$ period. As a pendulum, it means that the equivalent bob always approaches the top position during that time. The probability tree in Fig. 11(c) presents two stages:

(i) For the first stage, we divide the particles into two populations based on the sign of p_x. When starting from a particle distribution at rest, each sign is as likely as the other, and the probabilities to approach an X point from the left or from the right are both equal to 0.5.

(ii) The second stage is the coin toss at the boundary. A particle has 50% chance to cross the border and then move by $+1$ bucket if its momentum is positive, or move by -1 bucket if it is negative. Otherwise, it just stays in its bucket, but the direction of its momentum gets reversed.

Overall, at each event, this simple analysis shows that the random variable X_i [associated with the particle displacement at event (i)] has a 50% probability to remain in its bucket ($\mathcal{P}_0 = 0.5$ for $X_i = 0$) and a 25% crossing probability in each $+$ or $-$ direction ($\mathcal{P}_{\pm 1} = 0.25$ for $X_i = \pm 1$). Let us denote as D the probability distribution of X.

We have numerically checked these probabilities in the case of the simulation of Fig. 11(a), and we find $\mathcal{P}_0 \simeq 0.54$ and $\mathcal{P}_1 \simeq \mathcal{P}_{-1} \simeq 0.23$ [see the bar chart in Fig. 11(b)]. The slight discrepancy with the model comes from deeply trapped particles in the small stable islands, for which $|v_x| \ll c$. Such particles never come close to a bucket boundary and thus never experience a "coin toss" event. They stably remain close to an electric field node for many periods [e.g., the light blue trajectory in Fig. 11(a) after $7.5\,T_0$]. In the limit $a_0 \gg 1$, the stable island area totally shrinks, and numerical results get closer to the model. For example, for a simulation with $a_0 = 10$, we find $\mathcal{P}_0 \simeq 0.506$ and $\mathcal{P}_1 \simeq \mathcal{P}_{-1} \simeq 0.247$.

B. Temporal evolution of the spatial distribution

Let us now determine the distribution function of a particle's position $Y_n = \sum_{i=1}^{i=n} X_i$ after a large number of independent events n, assuming that each of the random particle displacements X_i is independent and identically distributed (with the probability law D established in the previous paragraph). In the following, we denote $\mu = 0$ the mean and $\sigma = \sqrt{2}$ the standard deviation of D.

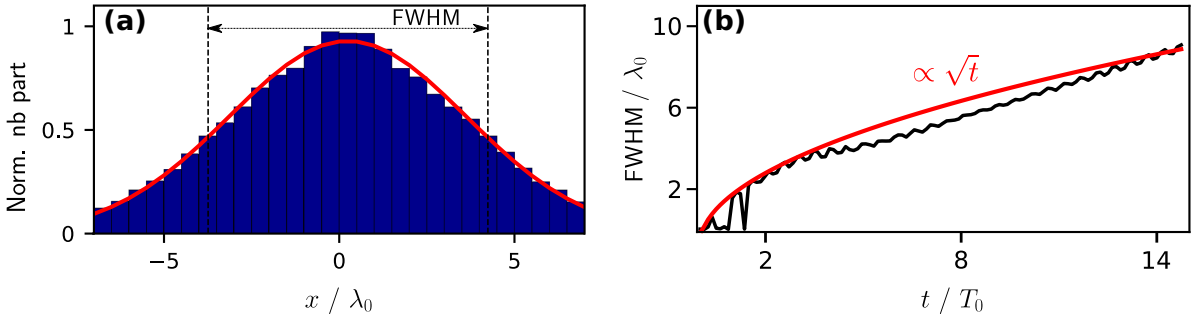

FIG. 12. Distribution of particle positions for $n = 18$. In panel (a), the electron positions are plotted as a 1D histogram at $t = 9T_0$ for the same simulation as in Fig. 11. Each histogram bar corresponds to a magnetic bucket. On top of the histogram is plotted a red line corresponding to the theoretical Gaussian distribution written in Eq. (42). In panel (b), we plot the evolution of the full width at half-maximum (FWHM) of the distribution of panel (a) along time as well as a function varying as $\sqrt{t}$.

According to the central limit theorem, when $n \gg 1$, the normal distribution $\mathcal{N}(n\mu, n\sigma^2)$ is a good approximation of the probability distribution of Y_n, yielding

$$P\left(Y_n = \sum_{i=1}^{i=n} X_i = x\right) = \frac{1}{\sqrt{2\pi n}\sigma} \exp\left[-\frac{1}{n}\left(\frac{x-\mu}{4\sigma}\right)^2\right], \tag{40}$$

i.e.,

$$P(Y_n = x) = \frac{1}{\sqrt{4\pi n}} \exp\left[-\frac{x^2}{4n}\right]. \tag{41}$$

Using $t_n = nT_0/2$, one finally gets

$$\mathcal{P}(Y_n = x) = \sqrt{\frac{T_0}{2\pi t_n}} \exp\left(-\frac{x^2}{Dt_n}\right) \quad \text{with } D = \frac{\lambda^2}{2T_0}. \tag{42}$$

The particle distribution thus approaches a Gaussian distribution at large n. Its expectation is of course zero, since we start from a population centered around $x = 0$, and its standard deviation scales as $\sqrt{n}$ (i.e., $\sqrt{t_n}$), which is characteristic of a *normal diffusion*.

In Fig. 12(a), the particle positions for the same simulation as in Fig. 11 at $t = t_{18} = 9\,T_0$ are plotted as a dark blue histogram along with the theoretical Gaussian distribution pictured as a red line. As one can see, the model agrees well with PT simulation results. In Fig. 12(b), we now plot the full width at half-maximum (FWHM) of the spatial distribution of electrons at each time step, and we compare this result to the standard deviation predicted by the model ($\propto\sqrt{t_n}$). The evolution of the particle positions in space is thus properly described by a simple Brownian motion.

This section closes our study dealing with electron motion in two counterpropagating waves. Let us now study the case of electron dynamics in electromagnetic waves crossing at an angle of incidence, and show how this can affect the electron dynamics. Such conditions are more representative of the ones used in most laser-matter experiments.

VI. INFLUENCE OF THE CROSSING ANGLE BETWEEN LASER BEAMS

All results presented so far assumed that the two plane waves were counterpropagating. This is not necessarily the case experimentally, for instance in laser-plasma interaction experiments. In this section, we introduce an angle $\alpha \neq \pi$ between the two waves (Fig. 13) and investigate how this affects the electron dynamics. As before, electrons are assumed to be initially at rest. We first show how a Lorentz transformation to a new reference frame [24] makes it possible to bring this configuration back to the case of two counterpropagating waves, and to thus partially exploit the analysis of the previous sections. This is inspired by a similar approach commonly used to analyze the interaction of a laser beam with the surface of a dense plasma at oblique incidence.

A. Equations for the electron dynamics

Starting from the configuration shown in Fig. 13(a) in the laboratory frame, we consider the Lorentz transformation to a new, so-called boosted frame moving along axis z with a velocity $v_d = c\cos\varphi$, corresponding to a Lorentz factor $\gamma_b = (1 - v_d^2/c^2)^{-1/2} = 1/\sin\varphi$.

In this new frame, it can easily be shown that the two waves are now propagating in exactly opposite directions, as considered in the previous sections. However, two main differences arise:

(i) Due to the effect of the boost on spatial and temporal scales, the laser angular frequency and wave vector are rescaled by a factor $1/\gamma_b$, $\omega_0' = \omega_0 \sin\varphi$ and $k_0' = k_0 \sin\varphi$.

(ii) Electrons that were initially at rest in the laboratory frame now have an initial velocity $v_d = c\cos\varphi$ in the boosted frame, in the direction z normal to the wave propagation direction.

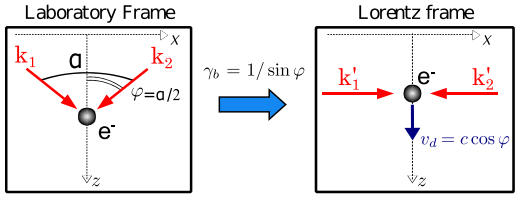

FIG. 13. Lorentz transformation for the analysis of non-counterpropagating configurations in the laboratory frame. We define $\varphi = \alpha/2$, as displayed in this figure. For two counterpropagating waves, $\alpha = \pi$ and $\varphi = \pi/2$. The y axis is normal to the figure plane.

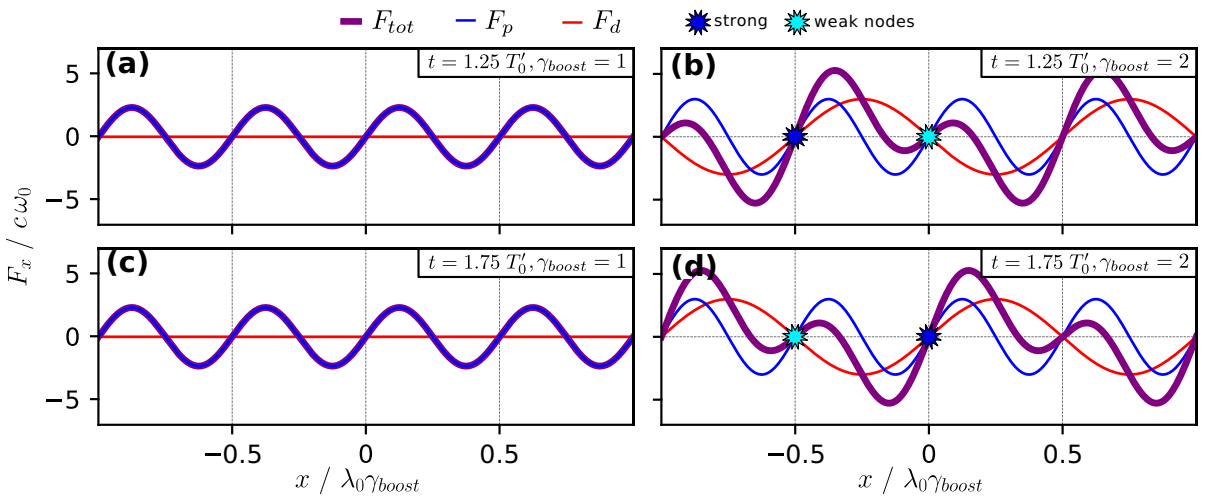

FIG. 14. Spatial profile of the different forces at various times, for two angles of incidence. For each panel, we plot three forces as a function of position in the boosted frame. The different times and γ_b are reported in the labels. The vertical dashed lines indicate the positions of magnetic field nodes. In the non-counter-propagating case, they alternatively switch from strong to weak and vice versa every half laser period.

The second point is particularly important here, because it will modify the derivation of equations of motion compared to what was done in Sec. II. Indeed, the drift velocity v_d corresponds to an initial transverse momentum:

$$\begin{aligned} p_{z,|t=0} &= m\gamma_b v_d \\ &= mc\ \tan\theta_i = mc\ \cot\varphi. \end{aligned} \tag{43}$$

As a result, the conservation of the transverse canonical momentum in the boosted frame now reads

$$\begin{aligned} p_y &= eA_y, \\ p_z &= eA_z + p_{z|t=0} = eA_z + mc\ \cot\varphi. \end{aligned} \tag{44}$$

This should be compared to Eq. (6) obtained in the counter-propagating case. It is essential to keep in mind (see Fig. 13) that the axis z corresponds to the bisector of the two laser beams in the laboratory frame, and is thus contained in the plane defined by the two k-vectors of these beams in this frame, while y is the direction normal to this plane. We are interested in the electron dynamics along x, the propagation axis of the waves in the boosted frames.

With a derivation similar to that of Sec. II, but now with the new expression of p_z, it yields

$$\begin{aligned} &\frac{d^2x}{dt^2} + \frac{e^2}{2m^2\gamma^2}\left(\frac{\partial}{\partial x} + \frac{\dot{x}}{c^2}\frac{\partial}{\partial t}\right)\left(A_y^2 + A_z^2\right) \\ &\quad + \frac{ec}{m\gamma^2}\cot\varphi\left(\frac{\partial}{\partial x} + \frac{\dot{x}}{c^2}\frac{\partial}{\partial t}\right)A_z = 0. \end{aligned} \tag{45}$$

This should be compared to Eq. (10) for the counter-propagating case. When the two waves are not exactly counterpropagating ($\varphi \neq \pi \Rightarrow \cot\varphi \neq 0$), a third term thus comes into play in the equation of motion. This terms is proportional to $\cot\varphi$, and it depends on the first-order derivatives of A_z, the component of the vector potential in the incidence plane of the two beams. In the boosted frame, this new force along x originates from the $v_d \times B_y$ term, where v_d is the constant drift velocity along z. Physically, this accounts for the force associated with the E_x component of the laser E fields in the laboratory frame.

A_y and A_z are both oscillating at frequency ω_0', while their squares are oscillating at the frequency $2\omega_0'$. We note that this interplay of two driving forces at different frequencies usually tends to reduce the chaos threshold. In the next subsections, we will analyze the electron dynamics for different laser beam configurations. Similarly to Sec. III, for the sake of simplicity we will restrict our analysis to the nonrelativistic limit of the equation of motion, which now reads

$$\frac{d^2x}{dt^2} + \frac{e^2}{2m^2}\frac{\partial A^2}{\partial x} + \frac{ec}{m}\cot\varphi\frac{\partial A_z}{\partial x} = 0, \tag{46}$$

where $A^2 = A_y^2 + A_z^2$. This can be compared with Eq. (11) in the counterpropagating case.

1. Electron motion in two L/L waves

We first consider the case of two linearly polarized waves. Many different configurations are possible depending on the polarization direction of each wave, but two cases are particularly important and instructive.

The simplest case is when both waves are linearly polarized along the y axis, perpendicular to the incidence plane of the two beams. Then $A_z = 0$, and Eq. (46) is identical to Eq. (11) regardless of the angle between the two waves. The particle dynamics in this case is hence similar to the counterpropagating case, with an additional drift along z in the boosted frame.

The situation gets more complex when the two waves are polarized along the z-axis, i.e., in the incidence plane of the two waves. Replacing A_z by its value given in Eq. (23) leads to the equation of motion

$$\begin{aligned} &\frac{d^2x}{dt^2} - \underbrace{a_0^2c^2k_0'\sin(2k_0'x)[1-\cos(2\omega_0't)]}_{F_p} \\ &\quad - \underbrace{2a_0c^2k_0'\cot\varphi\sin(k_0'x)\sin(\omega_0't)}_{F_d} = 0. \end{aligned} \tag{47}$$

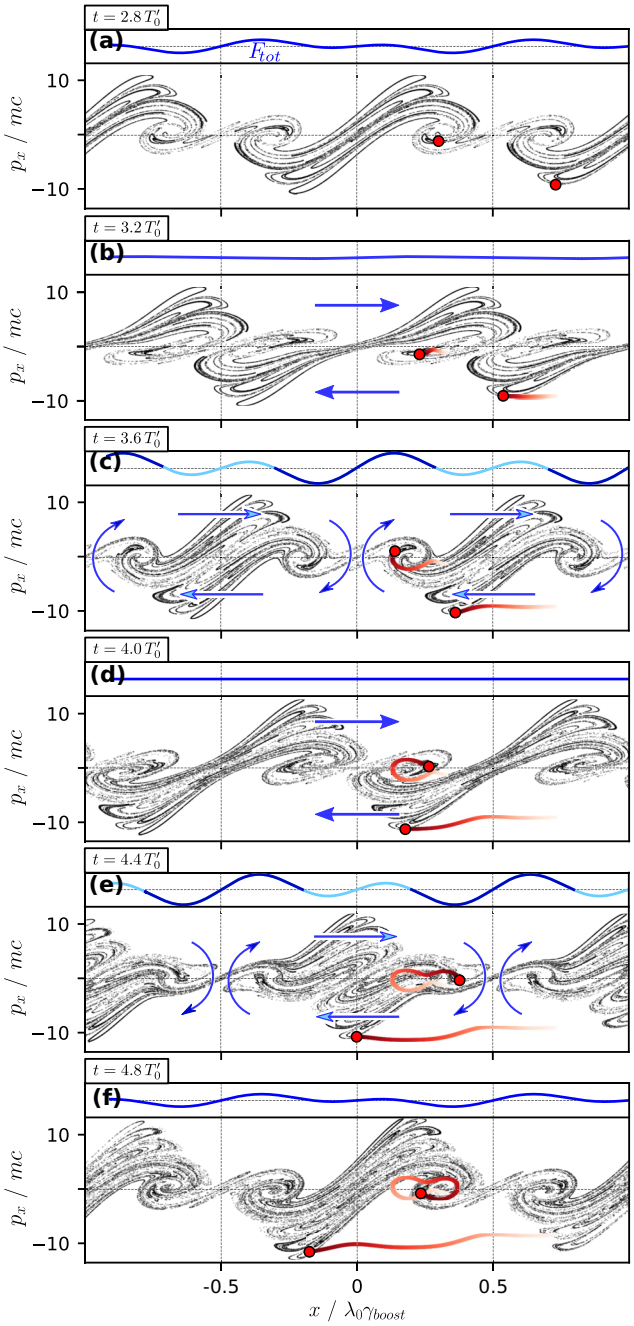

FIG. 15. Temporal evolution of the phase-space distribution of particles in the L/L case in oblique incidence. Same as Figs. 5 and 6 but with an angle of incidence $\varphi = 30^\circ$. Each panel corresponds to a snapshot of the distribution in phase space for $a_0 = 3$ at different times. On top of each panel, we plot the corresponding spatial profile of F_{tot}, with different shades of blue to highlight strong (dark) and weak (light) nodes.

The total force, F_{tot}, is a combination of two forces: F_p, the ponderomotive force (same force as in two counterpropagating cases), and a new force, F_d, which we call the *drifting force*, the magnitude of which depends on φ. Two limiting regimes can be identified:

(i) When $\cot\varphi \ll a_0$, $F_p \gg F_d$ and the dynamics is similar to that of the counterpropagating laser waves studied in the previous sections.

(ii) When increasing $\cot\varphi$ such that $\cot\varphi \gg a_0$, $F_p \gg F_d$, and the particle dynamics is now dominated by a force oscillating at a characteristic frequency ω_0'. This limit corresponds, for instance, to $\varphi \lesssim 84.3^\circ$ for $a_0 = 0.1$, and $\varphi \lesssim 18.4^\circ$ for $a_0 = 3$.

In between these two extremes, the two forces are of comparable magnitude. To analyze the effect of the combinations of these two forces F_d and F_p on the particle dynamics, we plot these two components as well as the total force $F_{\text{tot}} = F_p + F_d$ in Fig. 14 for $\varphi = 90^\circ$ (counterpropagating case, left panels) and 30° (right panels), at two different times separated by half a wave period. In these plots, position x and time t are, respectively, normalized to the wavelength $\lambda_0' = \lambda_0\gamma_b$ and period $T_0' = T_0\gamma_b$ of the wave in the boosted frame. Using this convention, the locations, in the boosted frame, of the field nodes introduced in the previous sections are identical to the counterpropagating case: electric field nodes are at $k_0'x = \pi/2 + n\pi$ $(\forall n \in \mathbb{Z})$ and magnetic field nodes at $k_0'x = n\pi$.

As in the counterpropagating case, the force F_p is $\lambda_0'/2$-periodic in space and does not depend on φ. At a given position, its sign does not change in time but its amplitude varies periodically with a period of $T_0'/2$. When $\varphi \neq \pi$ the force F_d comes into play and modulates F_p. It varies in time and space at half the frequency of F_p: it is λ_0'-periodic in space, and changes in time not only in amplitude but also in sign with a period of T_0'.

The key effect of this new force is to introduce what we call *strong and weak magnetic nodes*, separated by a distance $\lambda_0'/2$. A strong node [dark blue stars in Figs. 14(b)–14(d)] occurs when $|\partial F_{\text{tot}}/\partial x| \gg 0$. In contrast, a weak node [light blue stars in Figs. 14(b)–14(d)] occurs when $|\partial F_{\text{tot}}/\partial x| \simeq 0$. Each magnetic node alternatively switches from strong to weak and vice versa every $T_0'/2$ due to the different time dependence of F_p and F_d [cf. Fig. 14(b) versus 4(d)].

Figure 15 now analyzes the dynamics of particles in phase space in this configuration, using the same type of representation as in the counterpropagating case (see Figs. 5–7). The evolution of the phase-space distribution can again be decomposed as a periodic sequence of stretching and folding stages. This sequence is more complex than in the counterpropagating case, with two different spatial and temporal periods now coming into play.

A stretching stage over the entire phase space occurs when $F_{\text{tot}} \simeq 0$ [Figs. 15(a) and 15(b)]. A quarter of a period later [Fig. 15(c)], a folding phase occurs around strong magnetic nodes, where the spatial gradient of F_{tot} is strong such that initially neighboring particles tend to diverge. In contrast, a stretching phase is simultaneously ongoing around weak nodes, where both F_{tot} and its spatial gradient are weak such that particles follow quasiballistic trajectories. Half a period later, and after another global stretching phase [Fig. 15(d)], the same process occurs again, but the positions of weak and strong nodes are now swapped [Fig. 15(e)].

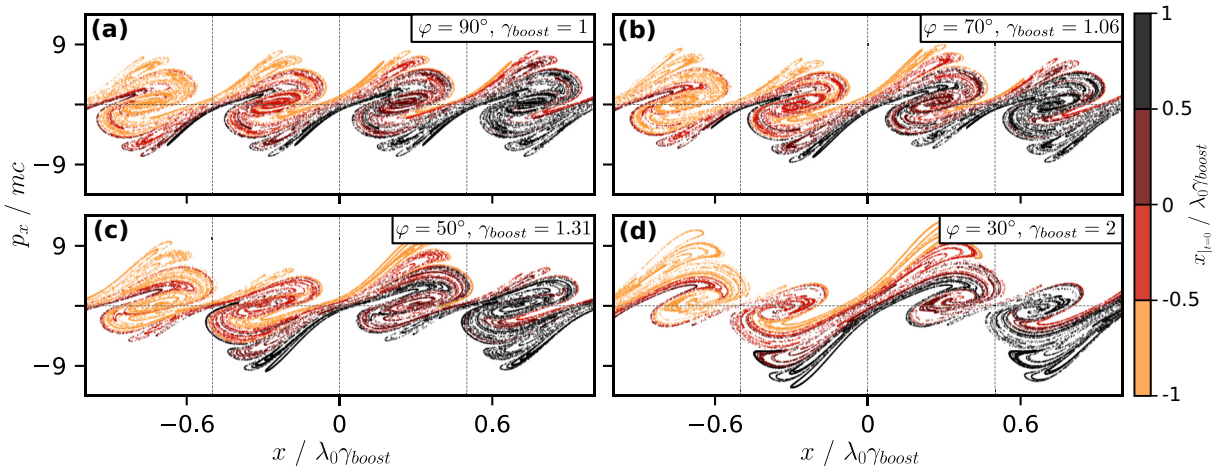

FIG. 16. Phase-space distribution of particles in L/L configuration at a fixed time for different angles of incidence. Each panel represents the electron distribution in phase space at $t = 2.8\ T_0'$ and $a_0 = 3$ for different angles of incidence indicated in the labels. As before, the different colors encode the initial positions within buckets.

This more complex stretching and folding process leads to particle diffusion in phase space and chaotic dynamics. Examples of particle trajectories in phase space are displayed in red in Fig. 15 for one particle trapped in a magnetic bucket and one circulating particle.

The influence on phase-space distributions of these complex dynamics is illustrated in Fig. 16, which displays such distributions for $a_0 = 3$, and φ gradually varying from 90° to 30°. As φ decreases, the spatial period of the phase-space distribution gradually changes from $\lambda_0'/2$ to λ_0', and a "butterflylike" structure appears due to the combination of the two forces and the spatiotemporal alternation of weak and strong nodes.

2. *Electron distribution in two circularly polarized waves*

We finally turn to the RHC/LHC configuration. As a reminder, this case was integrable in the Liouville sense when $\varphi = 90°$. However, we now show that this is no longer true in the non-counter-propagating case.

The vector potential is now given by Eq. (17), and the nonrelativistic equation of motion thus reads

$$\frac{d^2x}{dt^2} - \underbrace{a_0^2 c^2 k_0' \sin(2k_0' x)}_{F_p} + \underbrace{2a_0 c^2 k_0' \cot\varphi \sin(k_0' x)\sin(\omega_0' t)}_{F_d} = 0. \tag{48}$$

The first two terms constitute a simple pendulum equation. As soon as $\varphi \neq 0$, it gets perturbed by the third term, F_d, identical to that of the L/L case.

Figure 17 displays the phase-space distribution of particles at a fixed time for different crossing angles. As expected, the particle dynamics are not chaotic in Fig. 17(a) when $\varphi = 90°$. But as soon as φ is reduced, particles escape from their initial bucket, and color mixing is observed. This is a clear indication of the development of chaotic dynamics.

It is interesting to note that for small values of φ, the phase-space distribution becomes very similar to the ones obtained

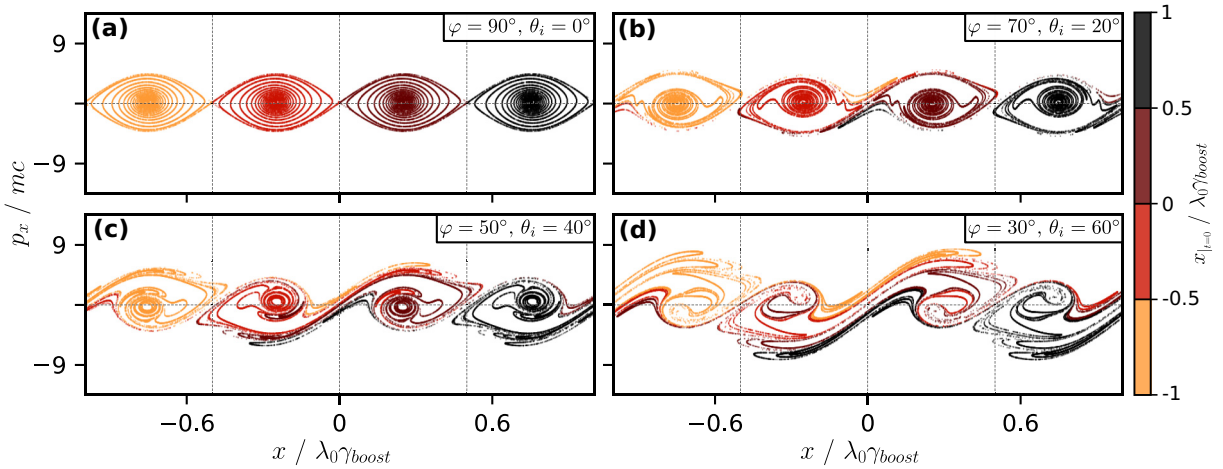

FIG. 17. Phase-space distribution of particles in RHC/LHC configuration at a fixed time, for different angles of incidence. Same as Fig. 16 but for a different laser polarization.

in the L/L case [see Fig. 17(d) versus Fig. 16(d)]. This is because as $\varphi \to 0$, $F_d \gg F_p$, and the equations of motion for the L/L and RHC/LHC cases become identical.

VII. CONCLUSION

In this work, we demonstrated that the equations governing a charged particle dynamics in colliding waves can be reduced to equations of simple pendulums, which exhibit predictable or chaotic motion depending on the wave polarizations. In particular, for two linearly polarized waves we showed that particle motion is similar to that of a forced pendulum, known as Kapitza's pendulum, which can exhibit chaotic properties.

Based on the analysis of the pendulum motion in phase space, we showed that chaos arises in electron motion through a stretching and folding mechanism, and we developed a simple model for this mechanism. Thanks to this first model, we were able to very accurately predict chaos thresholds. We then developed a random walk model for electron motion thanks to which we can now predict stochastic heating features as a function of the wave configuration.

Finally, using a simple Lorenz boosted frame transform, we generalized our analysis to the case of an arbitrary angle of incidence between two colliding waves, and we showed that stochasticity increases with the angle of incidence φ of the crossing angle of the laser waves.

[1] J. T. Mendonça and F. Doveil, J. Plasma Phys. **28**, 485 (1982).
[2] J. T. Mendonça, Phys. Rev. A **28**, 3592 (1983).
[3] J.-M. Rax, Phys. Fluids B **4**, 3962 (1992).
[4] A. Bourdier, D. Patin, and E. Lefebvre, Physica D **206**, 1 (2005).
[5] J. Faure, C. Rechatin, A. Norlin, A. Lifschitz, Y. Glinec, and V. Malka, Nature (London) **444**, 737 (2006).
[6] C. Rechatin, Accélération d'électrons dans l'interaction laser-plasma: développement et caractérisation d'un injecteur optique, Ph.D. thesis, Ecole Polytechnique X, 2009.
[7] L. Chopineau, A. Leblanc, G. Blaclard, A. Denoeud, M. Thévenet, J. Vay, G. Bonnaud, P. Martin, H. Vincenti, and F. Quéré, Phys. Rev. X **9**, 011050 (2019).
[8] S. Hüller, A. Porzio, J.-C. Adam, and A. Héron, Phys. Plasmas **26**, 083107 (2019).
[9] We do not consider the intensity regime where quantum electrodynamic effects come into play.
[10] Z.-M. Sheng, K. Mima, Y. Sentoku, M. S. Jovanović, T. Taguchi, J. Zhang, and J. Meyer-ter Vehn, Phys. Rev. Lett. **88**, 055004 (2002).
[11] J. W. Yoon, Y. G. Kim, I. W. Choi, J. H. Sung, H. W. Lee, S. K. Lee, and C. H. Nam, Optica **8**, 630 (2021).
[12] D. Escande, Phys. Rep. **121**, 165 (1985).
[13] J.-M. Rax, *Mécanique Analytique: Adiabaticité, Résonances, Chaos* (Dunod, 2020).
[14] P. Kapitza, Sov. Phys. JETP **21**, 588 (1951).
[15] P. Kapitza, Usp. Fiz. Nauk **44**, 7 (1951).
[16] S. H. Strogatz, *Nonlinear Dynamics and Chaos: With Applications to Physics, Biology, Chemistry, and Engineering* (CRC, Boca Raton, FL, 2015).
[17] C. K. Birdsall and A. B. Langdon, *Plasma Physics Via Computer Simulation* (CRC, Boca Raton, FL, 2018).
[18] R. W. Hockney and J. W. Eastwood, *Computer Simulation using Particles* (CRC, Boca Raton, FL, 2021).
[19] At $t = 0$, $1 - \cos(2\omega_0 t) = 0$, and at $t = T_0/4$, $1 - \cos(2\omega_0 t) = 2$.
[20] E. Meissner, Schweiz. Bauzeit. **72**, 95 (1918).
[21] A. P. Markeev, Nonlin. Dyn. **7**, 531 (2011).
[22] A. Markeev, Int. J. Non Linear Mech. **73**, 12 (2015).
[23] A. A. Burov and V. I. Nikonov, Int. J. Non Linear Mech. **110**, 26 (2019).
[24] A. Bourdier, Phys. Fluids **26**, 1804 (1983).